

JUN 30 1945

6443
343
-47

NATIONAL ADVISORY COMMITTEE FOR AERONAUTICS

TECHNICAL MEMORANDUM

No. 1078

EXPERIMENTAL AND THEORETICAL INVESTIGATIONS

OF CAVITATION IN WATER

By J. Ackeret

Eidgenössischen technischen Hochschule in Zürich, 1930



Washington
May 1945

N A C A LIBRARY
LANGLEY MEMORIAL AERONAUTICAL
LABORATORY
Langley Field, Va.



3 1176 01440 7846

NATIONAL ADVISORY COMMITTEE FOR AERONAUTICS

TECHNICAL MEMORANDUM NO. 1078

EXPERIMENTAL AND THEORETICAL INVESTIGATIONS
OF CAVITATION IN WATER*

By J. Ackeret

SUMMARY

The cavitation in nozzles on airfoils of various shape and on a sphere are experimentally investigated. The limits of cavitation and the extension of the zone of the bubbles in different stages of cavitation are photographically established. The pressure in the bubble area is constant and very low, jumping to high values at the end of the area. The analogy with the gas compression shock is adduced and discussed. The collapse of the bubbles under compression shock produces very high pressures internally, which, according to more recent conceptions, ^{may be} ~~are~~ contributory factors to corrosion. The pressure required for purely mechanical corrosion is also discussed.

I. GENERALITIES

1. Preliminary Remarks

In hydrodynamics it is generally permissible to treat water and the majority of liquid fluids as incompressible fluids. Even at the highest pressures attainable (of the order of magnitude of 1000 m of water) the density of water is only about 1/2 percent higher than normal. So, while the high-pressure side scarcely holds any surprises in store, the zone of low pressures involves one important

*"Experimentelle und theoretische Untersuchungen über Hohlraumbildung (Kavitation) im Wasser." Eidgenössischen technischen Hochschule in Zürich (Berlin), 1930.

limit: the saturation pressure of vapor. Once the pressure reaches this value during flow, the fluid loses its homogeneity and enters the phase of fluid and gaseous mixture, whereby the gaseous phase, in general, consists of a mixture of other gases. This is termed "cavitation."*

It was hardly to be expected that the complicated phenomena would be studied with special interest from the physical point of view, and it has been, in fact, unbelievably neglected, despite the fact that in principle it was well known.

Engineering necessities finally forced the resumption of the problem about two decades ago; but today, the matter has already reached the stage where cavitation has a decisive influence on the design of hydraulic machinery and defines the limits of technical possibilities.

Turbines, as is known, have been built for over a hundred years, but it remained for the trend toward high-speed engines to discover the fundamental difficulties of cavitation, just as the introduction of the steam turbines on ships led to the most disagreeable surprises because cavitation became especially apparent at the higher propeller revolutions per minute.

Cavitation nearly always increases the losses, lowers the efficiency, and reduces the transferable energy. But it may also be accompanied by especially disagreeable effects, the dreaded corrosion - that is, spongelike pitting which frequently occurs very severely in the most unexplainable way and which, even today, has never been definitely explained.

The present report is an attempt at a reliable description of cavitation in water and a rational explanation of the observations. Admittedly, the tumultuous behavior of all cavitation phenomena makes the use of average values unavoidable; furthermore, the many concurrently acting effects, such as heat conduction, capillarity, friction, evaporation, and diffusion perhaps

*Even before vaporization dissolved gases are separated at low pressure (Henry's law), although usually small in amount compared with the vapor masses released on reaching vapor pressure. An important exception is, of course, strongly carbonated water.

always will have to be classified according to order of magnitude of effect and only the strongest terms retained. Even so, the problem becomes difficult enough mathematically.

The investigations, at first only preliminary studies, extended over several years.

The preliminary tests, described in a short note (reference 1), were carried out in the Institute of Applied Mechanics at Göttingen. They served as a basis for the design of a larger experimental cavitation research plant constructed in the hydrodynamic laboratory of the Kaiser Wilhelm Institute for Flow Research, Göttingen, ~~and~~ with which the first results described hereinafter were obtained.

2. The Appearance of Very Low Pressures in Fluids

Consider, for the present, irrotational fluid motions - that is, a velocity potential Φ . Then the pressure equation (reference 2) for incompressible fluids reads:

$$p = p_0 - \frac{\rho}{2} c^2 - \rho \frac{\partial \Phi}{\partial t} \quad (1)$$

where

$$c = \sqrt{u^2 + v^2 + w^2} \quad \text{velocity}$$

$$\rho = \frac{\gamma}{g} \quad \text{density}$$

$$p \quad \text{absolute pressure}$$

In the stationary case equation (1) becomes the Bernoulli equation

$$p = p_0 - \frac{\rho}{2} c^2 \quad (1a)$$

If at any point the velocity becomes

$$c = \sqrt{\frac{2p_0}{\rho}} \quad (2)$$

p becomes zero at that point, and cavitation sets in. It actually occurs even at lower velocity because on reducing the pressure the dissolved gases are liberated, and on reaching the vapor tension the fluid begins to boil.

The term $\rho \frac{\partial \Phi}{\partial t}$ in equation (1) is of importance in nonstationary processes. For instance, take (fig. 1) a horizontal conduit with a plunger moving nonuniformly toward the right at speed u and drawing fluid from the large tank at the left. The pressure in the tank at the level of the plunger axis is $p_0 = B + \rho g h$ (B , barometric pressure, g , acceleration of gravity), and x is the abscissa of the plunger travel. Then

$$u = \frac{\partial \Phi}{\partial x}$$

and in a certain time interval

$$\Phi = u x$$

x being counted from the start of the pipe. Strictly speaking, the starting point A is a little forward of the start of the cylindrical piece, although no exact "orifice correction" is attempted.

Hence, at point x ,

$$\frac{\partial \Phi}{\partial t} = \frac{du}{dt} x$$

and the nonstationary pressure portion

$$-\rho \frac{du}{dt} x$$

This portion of the pressure drops linearly, and even the total pressure may drop readily to zero at small accelerations, provided x is great enough.

If the fluid motion is not irrotational, then equation (1a) holds for the individual flow filament but not for the total fluid mass. If the flow is turbulent, the pressure itself fluctuates very rapidly in time and place. The introduction of the mean values of the flow quantities alone in the motion equations does not give the absolute

lowest pressures (necessary for the appraisal of the cavitation hazard) but higher pressures (as pointed out by R. von Mises).

Now it is of interest to know these pressure differences even if only approximate, since turbulent flow is a frequent occurrence in technical problems. For instance, suppose that on a linear flow of velocity U there is superposed a turbulent flow consisting of individual vortices rotating in the same direction (fig. 2), the vortex axes being arranged in a square screen of $2l$ mesh width, the rotation being in circles, the remaining corners being at rest relative to an observer moving with the basic velocity U . The velocity c is distributed parabolically.

Introducing $\frac{r}{l} = x$, gives:

$$c = 4c_{\max} (x - x^2)$$

The rotatory motion is readily deduced:

$$\frac{dp}{dr} = \rho \frac{c^2}{r} \quad \text{or} \quad \frac{dp}{dx} = \rho \frac{c^2}{x}$$

Integration gives for the pressure difference between the vortex core (p_1) and a point of the circumference (p_2)

$$p_2 - p_1 = \frac{4}{3} \rho c_{\max}^2 \quad (3)$$

Naturally these assumptions are quite arbitrary; but even so, the order of magnitude of the pressure differences should be correct, the more so as no assumptions need to be made regarding the length l . About c_{\max} , itself very little data are available. According to Burgers' measurements, it is about 0.05 in a certain case for c_{\max}/U . At the same time, this gives, however, a relatively unimportant pressure reduction, namely $2 \times \frac{4}{3} \times 0.05^2 = \frac{1}{150}$ of the velocity head $\frac{1}{2g} U^2$.

In very turbulent dead air (Kármán vortices), the relative velocity variations are, of course, much greater; the lowest pressures will have to be looked for in the strongly rotating vortices. This has been confirmed by experiment. (See sec. 4.)

Cavitation is readily produced in the great vortices leaving the tips of airfoils or ship propellers, the blade tips of high-speed water turbines (so-called slot cavitation) and the hubs of propellers and turbines. Flamm has secured some very interesting stereoscopic views of such vortices. (See reference 3.)

For wing vortices Prandtl (reference 4) gives as distance $l = \frac{\pi}{4} b$ (b , span; $r_1 = \frac{l}{9.16}$, radius of vortex core).

Disregarding the generally small natural motion of the vortices gives the pressure within the core as

$$p = p_a - \frac{\rho}{2} \frac{\Gamma_0^2}{4\pi^2 r_1^2} - \frac{\rho}{2} \frac{\Gamma_0^2}{4\pi^2 r_1^2} = p_a - \frac{\rho \Gamma_0^2}{4\pi^2 r_1^2}$$

if Γ_0 , circulation of the tip vortices; and p_a , pressure at great distance from the wing. With Prandtl's value this gives

$$p_a - p = \frac{\rho \Gamma_0^2}{b^2} 3.41$$

and finally, after posing Γ_0 according to the Kutta-Joukowski theorem:

$$\Gamma_0 = \frac{c_{a0}}{2} U t$$

where $c_{a0} = \frac{4}{\pi} c_a$; c_a , lift coefficients (reference 5, p. 32);

U , blade velocity relative to water; and t , blade chord in stream direction (blade length in turbines):

$$\frac{p_a - p}{\frac{\rho}{2} U^2} = c_{a_0} \frac{t^2}{b^2} 1.705 \quad (4)$$

c_{a_0} hereby refers to the center section (elliptic lift distribution); c_a is defined by equation (9).

Practical values are $c_{a_0} = 0.80$ and $\frac{t}{b} = \frac{1}{3}$; hence

$$\frac{p_a - p}{\frac{\rho}{2} U^2} = 0.12$$

In turbines this tip vortex occurs as a slot vortex. However, the slot cavitation is not summarily predictable on the basis of the preceding formulas because the vortex intensity is different and the natural motion of the vortices can hardly be overlooked. But even so, the values obtained with equation (4) appear to be in agreement, to some extent, with those obtained on the cavitation-turbine test stands.

On the hub vortex it is not always the evaporation that causes the cavitation. Air is separated even at much higher pressure than that of vapor saturation, whereby the backflow to the hub prevents the air from washing away. Besides, the centrifugal effect drives all bubbles occurring elsewhere toward the inside. Since the hollow spaces remain, there is sufficient time for the dissolved gases to become free.

The pressure in boundary layers is, to a sufficient degree of approximation, that of the adjacent undisturbed flow. A particle sticking deep enough in the boundary layer remains, however, comparatively much longer in the zones of low pressure than those flowing outside, so that energetic air is released and vapor is formed. It seems therefore not at all impossible that by partial removal (by suction) of the boundary layers the cavitation, while not being prevented, is, however, weakened in effect. Experiments are lacking in this respect.

The irrotational flow, known to be almost realized by

suitable body forms, is much influenced by Kirchhoff and Thomson's theorem: "if the flow is irrotational, the lowest pressure (the highest speed) always exists somewhere on the boundary walls, but not within the fluid."

Kirchhoff's proof is as follows (reference 2, p. 46 and reference 6):

Since at constant ρ

$$\Delta\Phi = \frac{\partial^2\Phi}{\partial x^2} + \frac{\partial^2\Phi}{\partial y^2} + \frac{\partial^2\Phi}{\partial z^2} = 0$$

Φ cannot have a maximum or minimum within the fluid, according to a known formula of the theory of functions.

But $\frac{\partial\Phi}{\partial x}$ also has this characteristic. Hence, there are always points of greater $\frac{\partial\Phi}{\partial x}$ in the proximity of a point

P, and of greater velocity - that is, lower pressure. The lowest pressure must therefore occur somewhere on the boundary.

This important theorem becomes more plausible from the following more circumstantial but less formal reasoning:

Take a point P on a stationary streamline (fig. 3). Plotting axes x, y, and z with x in the flow direction gives $u = c_p$, $v = 0$, $w = 0$.

Then the following statement must be proved: always there is at least one point in the proximity of P where $u > c_p$; in general, v and w then will be other than zero, so that $c = \sqrt{u^2 + v^2 + w^2}$ is even greater than at P. After writing $u - c_p = \delta u$, the existence of points with positive δu in proximity of P must be proved; P in a parallelepiped ABCDEFGH flat in stream direction is endorsed. Now, if δu , say, were negative everywhere - that is, the theorem invalid - it would mean that, aside from the principal flow, fluid would pass in negative direction through the two sides ABCD and EFGH. In that case, however, δu cannot be equal to 0 in P, as is readily apparent when the flow freed from c_p is

presented by suitably distributed sources and sinks on ABCD and EFGH, respectively, which is possible when the flow is irrotational. In order to obtain $\delta u = 0$ in P, sinks would have to be disposed on EFGH or sources on ABCD - that is, δu would have to be positive there, at least in some points.

Incipient cavitation is therefore to be expected particularly at points of highly convex walls, for instance, on the suction side of blades.*

This conclusion is fully confirmed in the tests with the previously cited important exception of spheres and cylinders in pronounced vortex formation, where cavitation occurs first in the cores of the detached vortices.

3. Behavior of Water at Reduced Pressure

At reduced pressure the detached gases are released first (preferably on rigid walls); then, after the saturation pressure is reached, the actual vaporization starts with the formation of bubbles.

In Van der Waals' phase diagram (fig. 4) this process corresponds to a motion from A toward B, etc. (appropriate heat input and removal to provide for the isothermal process). Normally the evaporation starts then at B. But it was found that B can be undercut in direction toward C. This requires a very pure, gas-free fluid in perfectly clean vessels. J. Meyers has treated this subject thoroughly. (See reference 7.). He not only succeeded in reaching zero pressure but also in producing tensile stresses σ_z in the fluid. For distilled water he obtained $\sigma_z = -34.0$ atmospheres, for ethyl ether,

*When bearing in mind the great water falls utilized today in power plants, it is readily apparent that even relatively small local "over speeds" are potential sources of cavitation. On the 1680-meter fall (Falls in Wallis) the pressure near the free jet nozzle orifice becomes zero when the local velocity exceeds the discharge velocity (177 m/sec) by only 0.3 percent. Such high-pressure nozzles must therefore be designed with considerable convergence in order that the pressure toward the mouth drops monotonically to atmospheric pressure.

-72.0 atmospheres; without that these figures should be regarded as natural limits, the maximum negative pressure being largely dependent upon contingencies.

Figuring with the reduced Van der Waals equation

$$\left(\pi + \frac{3}{\varphi^2}\right)(3\vartheta - 1) = 8\vartheta$$

where

π reduced pressure

φ reduced volume

ϑ reduced temperature

and assuming the critical quantities

$T_k = 647^\circ$ absolute $p_k = 224.2$ kilograms per square centimeter absolute

gives for the pressure minimum 0 (fig. 4) according to

$$\varphi_c^3 = \frac{(3\varphi_c - 1)^2}{4\vartheta}; \quad p_c = \left(\frac{8\vartheta}{3\varphi_c - 1} - \frac{3}{\varphi_c^2} \right) p_k \quad (5)$$

the following figures:

$t = 18^\circ$	$\sigma_z = -1075$ kilograms per square centimeter
50.5°	$= -900$
82°	$= -710$

These figures are considerably higher than Meyer's figures. Hence the maximum tensile stresses may be considered to be much greater than around 30 kilograms per square centimeter, even if the reduced equation for water is considered as not very reliable.

The tensile strength also can be considered from a different point of view. Visualize extremely small particles floating in the fluid or protruding from the boundary walls, and characterized by the radius r . It

is generally conceded that tearing as well as evaporation starts principally at such particles or protuberances. (See reference 7.) Reflecting that in this case the tearing consists of the separation of water from the surface of the particles and the bubble formed in this manner grows, the knowledge of the radius affords a relation for the maximum negative pressure. That is, with σ equal to surface tension and p equal to negative pressure:

$$2\pi r\sigma = \pi r^2 p$$

$$p = \frac{2\sigma}{r} \quad \text{or} \quad r = \frac{2\sigma}{p} \quad (6)$$

Assuming $\sigma = 72 \frac{\text{dyn}}{\text{cm}}$ and (according to Meyer) $p \approx 30 \times 10^6 \frac{\text{dyn}}{\text{cm}^2}$ the result is $r \approx 0.5 \times 10^{-5}$ centimeters - that is, an ultramicroscopic particle. The vapor pressure plays no essential part. Hence very fine impurities could, after all, be taken into consideration as a cause of the tearing at relatively low tensile stresses.

These considerations are of significance for the following reason: although it is certain that all industrial water contains so much of dissolved gases and impurities that it always tears with bubble formation, in the normal "static" tensile test, it does not, on the other hand, preclude the possibility that the tearing process requires a time interval which, in many practical cases, already is shorter.

In Bauer's experiments, for instance, (described elsewhere in the report) the water flowing past the sphere is under low pressure for about 0.6×10^{-5} seconds only. The water of the boundary layer, of course, is under low pressure longer. It would not be very surprising if they were actually accompanied by tensile stresses (even though of comparatively little extent). The author's experiments, so far, have been negative in this respect.

Once bubbles have been formed they become larger, because capillary tension drops quickly with the radius and the water evaporates. The rate of evaporation, however,

is wholly governed by the heat input in the bubble due to conduction, which renders the entire process quite complex.

II. EXPERIMENTS ABOUT THE FORMATION AND DEVELOPMENT OF CAVITATION

1. Preliminary Remarks

The experiments described hereunder were made in the Kaiser Wilhelm Institut for Flow Research at Göttingen. Their chief purpose was to collect sufficient visual data, which, at that time (1926-27), were very few. There may have been additional information in some progressive industrial concerns, but little has ever reached publication.*

The experiments included tests with closed channels, airfoils (such as employed for ship propellers and hydraulic turbines), spheres and cylinders. The cavitations observed disclosed many common features.

2. Tests on Closed Water Channels

A convergent-divergent channel offers a good opportunity for producing and observing cavitation in simple manner. According to Bernoulli's law, the lowest pressure (and hence cavitation) occurs in the narrowest part of the channel, and which is, according to Kirchhoff's theorem, at the walls.

If p_1 is the absolute pressure in the tank out of which the water flows, p_2 the barometric pressure, and p_m the pressure in the narrowest section, then

$$p_1 - p_m = \frac{\rho}{2} w_m^2$$

*Professor Dubs states that back in 1908 he had made experiments with convergent-divergent nozzles on the occasion of a report by Camerer (reference 8) published in Dinglers polytechn. Journal, 1902, p. 677. The results of his pressure measurements are similar to those described in pt. II, sec. 2. (See also reference 8.)

for potential flow and very approximately also for real fluids, because the losses are small in accelerated flow. In the adjoining divergent part of the channel, kinetic energy is changed back to potential energy (diffuser effect), but with substantially greater losses.

The pressure rise is

$$p_2 - p_m = \psi \frac{\rho}{2} (w_m^2 - w_2^2)$$

where ψ denotes the diffuser efficiency.

Cavitation starts at low p_m (of the order of magnitude of vapor pressure at corresponding temperature).

Since $p_m \approx 0$,

$$p_1 - p_2 = \frac{\rho}{2} \left\{ w_m^2 (1 - \psi) + \psi w_2^2 \right\} \quad (7)$$

and, since w_2 is small,

$$p_1 - p_2 = \frac{\rho}{2} w_m^2 (1 - \psi)$$

and, with $p_1 \approx \frac{\rho}{2} w_m^2$

$$p_1 = \frac{p_2}{\psi} \quad (8)$$

Since $p_2 \approx 10$ meters of water, $\psi \approx 0.7$, it requires only about 4.3 meters overpressure to produce cavitation. In fact, cavitation can be produced easily with the common water line of a house.

In a preliminary test on a nozzle with flat side walls, as illustrated in figure 5, the plotted pressure distribution curves were obtained. The pressure was recorded with orifices of 1/2-millimeter width on one of the curved flanks, the water flowing from a tank through the nozzle and a sheet-metal diffuser to the outside. The tank pressure was raised progressively which, at the same time, increased the throughflow quantity. This was measured directly with a rectangular tank as well as indirectly in good agreement with it from the tank pressure

drop to the narrowest section. The barometric pressure was 750.5 millimeters of mercury, the water temperature 10.4°C , and the corresponding vapor pressure 9.2 millimeters of mercury. At 11.0-meters-per-second mean velocity in the narrowest section, the pressure in the enlarged portion of the nozzle (flow from left to right) still rises normally, likewise at 13.1 meters per second. But at $w_m = 14.4$ meters per second a distinct divergence is noticeable; the pressure rise following the minimum is very flat, then climbs considerably. At still further increase of velocity the rise turns toward the right so that at 15 meters per second, for instance, it is entirely out of measuring range, and the pressure behind the narrowest section is almost constant. There is hardly any doubt that cavitation prevails; because the recorded minimum pressures lie, within the limits of error, in the region of vapor saturation pressure.

It soon became apparent that this behavior was typical and accordingly repeated itself on blades, and so forth. Observation through a glass window shows the fluid clear at 11 and 13 meters per second, but in the stages of forming a band of white foam on the sides of the nozzles at 14.4 and 15 meters per second. It extends just as far as the range of low pressure and disappears in the zone of pressure rise.

The phenomenon is not quiescent, the mercury manometers fluctuate irregularly. First of all the start of the separation was not locally defined and fluctuated erratically. So in these experiments and the subsequent ones the simple expedient of soldering 0.2-millimeter gage wires crosswise to the flow directly ahead of the narrowest section was preferred. The foam then appeared with great certainty at that point, and the entire process remained more uniform. Admittedly, the point of disappearance of the bubbles - that is, of the pressure rise - was never very accurately fixed; hence, all pressure readings present averages only.

After the first tests it was suspected that the disappearance of the bubbles and the pressure jump associated with it forms an analogy to the stationary compression shock (Riemann, Stodola (reference 9)). The subsequent tests served to confirm this supposition.

Then a new experimental apparatus was constructed (fig. 6), which differed from the first chiefly in the dimensions with a view to photographic and kinematographic recording (a relatively thin water sheet).

It consisted of a convergent-divergent channel with two flat sides, a minimum curvature of the other walls assuring a close approximation to a unidimensional flow. The setup was connected to the water line of the institute. A honeycomb was mounted ahead of the contraction. The actual test length of the rectangular cross section was of brass and so designed that the processes could be conveniently observed through two glass plates. In some pressure measurements one of the glass plates was removed, and a brass plate fitted with pressure leads $p_a, p_1 \dots p_{10}$. (See fig. 6.) The test orifices were of 1/2 millimeter diameter, the edges were not rounded off, though the burrs were carefully removed. U-tubes containing water on top of mercury in both legs served as manometers. (See fig. 7.) The leg on the external pressure side of the U-tube held the rubber tubing reaching into a tank filled with water, the level of which was on a level with the test point, so that height corrections were not necessary. At such pressure measurements the cavities which naturally also form in the test lines on the low-pressure side must be carefully taken into consideration; for the vapor pressure of the water is very accurately reached. All lines were made of glass so that the bubbles in the pipes could be observed and appropriate corrections be effected. Care was taken so that the low-pressure distances were disposed as flat as possible to keep those corrections to a minimum. The absolute pressure was recorded directly, from time to time, with a U-tube closed at one end and containing mercury. But the instrument did not prove as practical as anticipated, at first, because it also required height corrections, which, on the whole, were much greater than with the common U-tube.

The readings were taken when the pressure difference $p_a - p_0$, which is a measure for the throughflow quantity, remained constant for some time. This way even the minor pressure variations in the house water line did not become disturbing.

The divergent discharge pipe was fitted with a throttle valve and a simple regulating device by means of which, at constant throughflow, the absolute pressure in the

whole apparatus could be raised or lowered. The water was measured with a calibrated container.

First the pressure rise $p - p_a$ in the enlarged part (diffuser) of the test channel was measured at flow without cavitation and, in addition, computed from the cross-sectional dimensions according to Bernoulli's equation (fig. 8); the nondimensional formula $\frac{p - p_a}{q}$ was plotted as ordinate, whereby $q = \frac{\rho}{2} w_m^2$. The previously cited diffuser efficiency (or better, the degree of pressure conversion) for test point 8, for instance, is approximately:

$$\frac{(p_s - p_a)_{\text{observed}}}{(p_s - p_a)_{\text{computed}}} = 80.5 \text{ percent}$$

a value which is in agreement with experiments elsewhere. (See reference 10.)

As far as the narrowest section the losses are small, as seen from a comparison of the direct volumetric water measurements with those computed from the pressure drop $p_0 - p_a$, according to Bernoulli, if the inflow velocity at test point p_0 is allowed for in the calculation. The volumetrically defined water volume is 2.4 percent less and served in all subsequent calculations. The dynamic pressure therefore refers to the actual quantity of throughflow.

The pressure measurements at points 1 to 10 are given in table I and plotted in figures 9 and 10. As in all subsequent tables the pressure is expressed in meters of water column. The quantity of water in figure 9 was always around 1.47 liters per second, and 1.69 liters per second in figure 10. The character of both families of curves obviously is identical. It is plain that the six lower curves of figure 9 merge in proximity of the critical section - that is, that across this distance no change in flow condition takes place in spite of the variation in back pressure on the discharge end. So, notwithstanding further throttling, it was not necessary to change the inflow pressure p_0 (see table I) in order to

obtain the same throughflow of water. The pressure in the narrowest section does not increase until the back pressure is high; when, of course, the inflow pressure itself must be raised in order to assume the same throughflow quantity. (See table I, last line.) This behavior is perfectly analogous to that of the flow of gas through a Laval nozzle, where the throughflow quantity also does not change when the back pressure is changed. It is known that supersonic velocity prevails in the divergent part and that disturbances cannot react as long as the momentary sonic velocity remains exceeded at some point. Throttling produces the well-known Riemann-Stodola stationary compression shocks which approach the critical section as the back pressure is increased. Ultimately the shock reaches the narrowest section, every supersonic velocity disappears and the nozzle operates as diffuser.

Here the similarity of the visual phenomena is such that a natural temptation arises to push the analogy further and see whether the interval mechanism accompanying the gas shock also is related with the cavitation shock.

Here direct observation alone is decisive; so an attempt was made to render the processes in the nozzle visible.

Obviously, visual observation and ordinary photography with exposures of the order of magnitude of $1/10$ second afford only average values, since the cavitation phenomena are, in general, not uniform. Photographs of this type are shown in figures 22 to 26 and 32 to 33.

It became obvious that instantaneous photographs of very short exposures (10^{-5} to 10^{-6} sec.) should be taken by means of strong electric sparks. In this time interval an object moving with the water, such as a steam bubble, moves about 0.2 to 0.02 millimeter at a water speed of around 20 meters per second; hence, assures sufficient sharpness on the film. Obviously, the light of the spark loses much of its optical efficiency during its passage through glass plates and layers of water. For this reason, the dimensions of the test nozzle, as previously stated, were chosen comparatively small.

However, the cavitation boundary manifested fluctuations with widely varying frequencies; whereas relatively slow changes in the position of the shock area are

especially desirable for the appraisal of the pressure readings, since the mercury manometers used had quite slow natural oscillations and consequently indicated only average values even of those slow fluctuations.

In order to penetrate a little deeper, photographs were taken with 100 pictures per second, which at least explain the small frequencies. Despite its elementary character the setup employed proved satisfactory. The rim of a bicycle wheel was filled with paraffin, turned, and covered with a standard size film (about 2 m. long). The wheel was then placed in a lightproof box and driven from without by a small motor. The lens was taken from a small Ica-"Kinamo"-motion-picture camera. The original light source, sparks between copper tips, was given up after it was found that elektron (consisting largely of magnesium) gives very bright sparks. A focusing lens projected the light through the channel on to the film. The high-tension current was supplied by a small transformer connected to one phase of the alternating-current circuit and hooked in parallel with nine Leyden jars. Thus the sparking order was equal to twice the power source frequency - that is, about 100 per second. Unfortunately it was not always possible to achieve uniform arcing over; although that is more of an error in beauty than an actual impairment of the results.

Figures 11 and 12 show two enlarged film sections. The flow is from left to right; the bubble area is shown as the white shadow picture on the sides. The three pictures were taken at exact intervals of 1/100 second each. Figure 12 shows the foaming by slight throttling, and figure 11 with considerable throttling; here it has already retreated more toward the narrowest section.

Next, some closely spaced pressure orifices were drilled into one side (as in the preliminary test, fig. 5) for exploring the pressure distribution in the after portion of the foam area. The results are given in tables II and III, and figure 13. The orifices are numbered from 11 to 15 downstream, the pressure record is given in meters of water. The individual curves refer almost exactly to the same quantity of water; but the form strip extends unevenly as a result of different throttling. The top curve refers to cavitation-free throughflow; the next ones refer to throughflow at which the shock in average time reaches, according to direct observation, the text orifices 11, 12, 13, 14, and 15, which are spaced 3

millimeters apart, and as far as points 16, 17, and 18, which are 3, 6, and 9 millimeters, respectively, downstream from test point 15.

It is readily seen that the pressure rise $p_{15} - p_{11}$ is considerably greater when the shock occurs in the zone of the test length than when it does not reach it or even leaves it behind altogether. Hence the assumption that the end of the foam strip is the location of a pressure jump appears to be confirmed. From these findings various conclusions as to the form and size of pressure jump are permissible.

Figure 14 shows $\frac{p_n - p_{11}}{q}$ where p_n is the pressure at one of the test points 12 to 15 and $q = \frac{\rho}{2} w_m^2$ is the dynamic pressure, the mean range of the shock serving as abscissa. The test points are joined by curves, having a characteristic maximum.

Now, if the shock were an actual discontinuity in the pressure, entirely different curves would have to result. At a certain point, say, at 15, the pressure would have to be high almost constantly so long as the shock occurs in the positions 11, 12, 13, or 14. Then on passing through 15 there would be a sudden drop to zero (15 and 14 would have the same pressure). Likewise, the difference for shock positions upstream from point 11 would have to be small and assume the full amount suddenly on passing beyond 11. The curves would, in short, have to be rectangular.

But the shock fluctuates, according to the observations, back and forth over the test point; while the manometer indicates the time average of the pressure fairly accurately. This naturally blurs the relatively steep pressure rise and simulates a more continuous transition. The recorded pressure depends upon the time average as the high- or low-pressure zone downstream or upstream from the shock hovers over the test point. The curves of figure 14 afford an estimation if accompanied by data on the local fluctuation. In the case in question the position of the shock point was obtained from the film records at intervals of 1/100 second. A rough average was ± 3 millimeters—that is, twice the distance of two test orifices. It further is justifiable to assume that on the average

the shock oscillates back and forth at constant velocity. Then the frequency becomes subordinate for the subsequent considerations.

Figure 15 shows a form of pressure jump the back and forth swing of which to the amount of ± 3 millimeters is a fairly accurate picture of the pressure distribution, consisting essentially of three straight lines of different slope. Naturally the choice of slope and of the height of jump is somewhat arbitrary; but even so, there are some restrictions.

Assuming this shock to swing ± 3 millimeters about the median position, or what is called the mean range (11 to 18), the average value of the pressure is readily computed graphically or mathematically. The ascending slope of the upper and lower straight piece are so chosen that the measured shock values at the extreme left or extreme right are correctly obtained, leaving only the slope and height of jump in the middle to be determined. Take, for example, a certain slope and amplitude and determine

$P_{12} - P_{11}$, and so forth; the result is a set of curves as shown in figure 14, which, however, must be reconciled as to scale and mutual position with the experimental curves. On the other hand, the use of the experimental curves to determine the two missing pieces results in the curve of figure 16, which actually is very similar to the experimental curve of figure 14 in many details.

The form of the pressure jump of figure 15 is thus quite plausible. Its theoretical interpretation is given elsewhere.

Hence, if a pressure jump extends over about 5 millimeters, it follows that an entrained floating particle or a steam bubble speeds through this zone at a rate of 20 meters per second within about $1/4000$ second. The unusual phenomena involved herein are discussed later.

3. Tests on Airfoils

It is to be expected that phenomena similar to those in divergent nozzles will also occur on the suction side of airfoils where, in general, a drop in pressure to minimum is followed by a pressure rise. The pressure side

is less involved since the pressure is not lower than on the suction side even at the locally confined regions of lower pressure. At higher negative angles of attack, of course, the bottom surface becomes the suction side; then the separation starts there first. On thick airfoils and at very low pressure, or at very high speed, the separation can occur on both sides simultaneously.

Cavitation on profiles is of greatest practical interest, especially on blades in cascade, such as used on ship propellers and hydraulic turbines. The study of single blades of itself would not be so important; nevertheless it seems advisable to explore the limiting case of very wide cascade spacing first. This case is treated more completely theoretically and is actually realized even on high-speed turbines and screws.

The airfoils must be studied in a perfectly closed tunnel; this involves wall disturbances which are negligible only when the airfoil dimensions are small compared to the wall distances. No special efforts, however, were made to avoid these effects in order to obtain airfoil dimensions which permitted the pressure measurements at the drilled holes. In preliminary tests, to be sure, it had been successfully attempted to make pressure records on the bounding side walls rather than on the airfoil itself and to extrapolate to the pressure on the airfoil. (See reference 1.)

But, quite apart from the trouble involved, it was difficult to fit the airfoil tightly enough without at least partial equalization of the pressure differences on suction and pressure side, with, of course, errors difficult to control. For most practical requirements systematic cavitation tests on cascades will be difficult to avoid. Besides, tests on turbine wheels and ship propellers are naturally of particular importance for the engineer, since he is ultimately interested in the total effect.

The airfoil tests were made in the new cavitation test plant of the Kaiser Wilhelm Institut for Flow Research, which operates with a completely closed circuit. (See fig. 17.) The centrifugal pump is located about 4 meters (13 ft) below the test stand to assure freedom from cavitation. The motive power is an adjustable direct-current motor of 20 horsepower. The 10-cubic-

meter tank serves to still the water and to remove the air bubbles before re-entering the test section. The space above the water can be evacuated or be put under higher pressure. This has the great advantage of being able to change the absolute pressure of the whole system at will, keeping the same speed (i.e., the same Reynolds number), so that the formation and the disappearance of the separation can be quickly and conveniently followed. The experimental pipe lines on the upper floor are shown in figures 18 and 19. The water leaves the tank through a 450-millimeter-wide fitting in which a honeycomb of 20-millimeter mesh is mounted. The tapering pieces ultimately narrow the cross section to a rectangle of 102.5 x 61.5 millimeters. All bends have a wide radius. After leaving the actual test section the water passes through an elongated diffuser.

The test section for wing studies is shown in figure 20. It consists of a square box with two round flanges. Solid brass plates or glass windows can be fitted on the two flat sides. Sealing the edges of the glass plates proved particularly difficult. Since the shocklike pressures deformed the glass plate, even putty did not prevent altogether the very disagreeable entry of the air from without, making it necessary to put the whole side plate under water. Then a small window set in the upper narrow side permitted spark illumination from above concurrently with observation through the side window. Another small window on top enabled the illumination from above by spark and observation of the suction side. The airfoil models extended freely from a brass body adjustable from the outside to any desired angular setting with respect to the water flow.

The airfoil sections investigated so far are shown in figure 21 as A, B, C, D, and E in order of thickness, A and B corresponding to airfoil sections 449 and 398 previously tested in the Göttingen wind tunnel. (See reference 5, pp. 76 and 82.) All profiles had 1/2-millimeter pressure orifices; the three thin profiles could accommodate only three orifices. The pressure was measured as customary with mercury manometers.

The study included:

- (1) Wind-tunnel tests on similarly enlarged models
- (2) Determination of pressure and water velocity at which separation sets in

(3) Pressure measurements on the surfaces in operation with and without cavitation.

The normal wind-tunnel measurements give (1) the cross-wind force: A normal to the velocity at great distance from the airfoil, (2) the drag W in direction of this flow, and (3) the moments M about a certain point.

The data are represented in nondimensional form defined by:

$$\left. \begin{aligned} A &= c_a \frac{\rho}{2} v^2 F \\ W &= c_w \frac{\rho}{2} v^2 F \\ M &= c_m \frac{\rho}{2} v^2 Ft \end{aligned} \right\} \quad (9)$$

where

ρ density

v undisturbed flow

F wing area (chord times width)

t chord

The moment reference point is arbitrarily chosen as the most forward point of the wing chord. The results are given in tables IV to VIII.

The angle of attack α_∞ is defined as the angle between the wing chord and the direction of undisturbed flow. All values are reduced to two-dimensional flow according to the Prandtl-Betz theory (reference 5, p. 36), which accounts for the effect of the free tips of the airfoils in a perfectly satisfactory manner.

The drag values of airfoils A and B manifest typical differences from C, D, and E. The drag for A and B varies little over a fairly wide range of angle of attack, while C, D, and E show a minimum at certain angles of attack. The thin sections have very low drag; but the ratio of

lift to drag $\left(\frac{l}{e}\right)$ of particular importance in practice, is, nevertheless, no more favorable than on the thicker airfoil sections.

The cavitation is especially evident when the pressure in the whole system is changed at constant velocity.

No disturbance is visible at high pressure; when the pressure drops, the spark light shows plainly visible individual bubbles at the surface in proximity of the leading edge. The bubbles are round, frequently also hemispherical, and from 1 to 4 millimeters in diameter. At this stage the upper side of the airfoil does not show many bubbles at one time (perhaps a dozen). As the pressure continues to drop the number of bubbles increases, which, under customary illumination, then appear as white foam. Figure 22 is a short time exposure of this stage on airfoil A; the white form reaches only up to a certain distance from the leading edge. Upon further pressure decrease (fig. 23) this shock moves backward in the same way as on the diffuser. (See fig. 14.)

The spark illumination then reveals a dense mixture of bubbles of varying sizes; the foam covered area changes rapidly in size and shape. But the outside appearance under permanent lighting is surprisingly well reproducible by simultaneous adjustment of outside pressure and velocity. Even then no separation of flow is involved, which sets in rather abruptly at still lower pressure (fig. 24) and which is also reproducible. In this particular case two distinct Helmholtz (reference 11) discontinuity surfaces as well as Rayleigh's flow about an oblique plate on the basis of Helmholtz's method were realized. In engineering, cavitation is usually identified with separation. But according to the present results it is permitted only at very low negative pressure.

The thin airfoils manifested similar phenomena, except that the start of separation is much more indeterminate, in accord with theory, which also predicts cavitation at the sharp leading edges at minimum velocity. (See figs. 25 and 26.) With the equipment available, it was impossible to reach separation on C, D, and E, because, at the low pressures necessary for this, the pump itself came into the cavitation zone and failed despite its low situation.

To fix these phenomena mathematically, some experiments were made on the basis of the following assumptions:

The letter P is any point on the airfoil surface;

w_∞ and p_∞ , respectively, are the velocity and pressure remote from the airfoil. With w denoting the velocity, the pressure at P is, according to Bernoulli:

$$p = p_\infty - \frac{\rho}{2} (w^2 - w_\infty^2)$$

Take, say, point P_m , where the pressure is lowest. Since the velocity existing at that point at equal angle of attack is proportional to velocity w_∞ :

$$w_m = w_\infty \alpha$$

with $\lambda = (\alpha^2 - 1)$ and $q = \frac{\rho}{2} w_\infty^2$

$$p = p_\infty - \lambda q \quad (10)$$

At incipient separation p will have a certain small value p_d . To each value of the dynamic pressure q there corresponds a pressure at which separation starts of

$$p_\infty = p_d + \lambda q \quad (11)$$

After measuring the dynamic pressure q as difference of $p_o - p_a$, a sufficiently close approximation is $p_a = p_\infty$. The result is then a linear relationship between p_∞ and q which can be checked. The appearance of the first bubbles is very much dependent upon circumstances (slight protuberances, etc.). It is therefore recommended to designate a more advanced stage which can be accurately adjusted, as "start," in this particular case the stage where the foam formation extends over the entire profile side and to about one-fourth of the chord. Then, if the pressure $p_a \approx p_\infty$ is adjusted in such a way that the shock always appears on the same place of the wing, and the recorded p_a is plotted against q , the solid dots of figures 27, 28, 29, and the values in tables IX and X are obtained. A straight line can always be drawn through the points, which, as it should be, does not

pass through the zero point but through the point p_d to the amount of 0.3 to 0.5 meters of water - that is, close to the vapor pressure of the water at the test temperatures.

The expectation was thus closely confirmed and on all airfoil sections.

Even more unusual is the fact that the advanced stages also afford a straight line variation of p versus q and are reproducible. For it might be suspected that, since at different velocities the bubbles have not the same dimensions, the shock areas would perhaps shift as a result of capillary forces. But the matter is substantially simple. Here also there is a p - q straight line and likewise one for the separation stage (on profiles A and B). All straight lines pass through exactly the same point. The (+) points denote the stage where the shock reaches the trailing edge (as in figs. 23 and 26). The small circles (o) denote the stage where separation just starts.

Graphical reproduction of all the test data was not deemed necessary, and the reader is referred to tables IX and X. It is expedient to indicate only the slope

$\frac{p_a - p_d}{q} = \lambda$ of the straight lines, as in table XI, which

distinctly shows the very important distance between incipient separation and separation of flow.

The slope and hence the danger of cavitation is greater on thick airfoils and at higher angles of attack.

Admittedly these experiments are not comprehensive enough to venture an answer to the question of best airfoil in respect to cavitation. To work without cavitation, pressure measurements in the wind tunnel are sufficient, but work with small cavitation requires drag measurements

in order to be able to assess $\epsilon = \frac{c_w}{c_a}$. It seems as if

the skin friction becomes less on first appearance of separation.

It was possible to record the pressure on the points at the suction side indicated in figure 21, which afforded merely a survey of the pressure distribution but no complete

curve, as it was impossible to accommodate any more pressure orifices within the confined space of the airfoil.

The results are given in tables XII and XIII; $p_o - p_a$ is again proportional to the dynamic pressure q ; all pressures are absolute in meters of water. The ratio p/q is also included.

Figure 30 gives as an illustration the pressure curves for airfoil A at $\alpha = 2^\circ$. Four stages were examined: (1) without cavitation, (2) shock at $1/2$ chord t , (3) at 1 chord t , and (4) separation. The pressure distribution is exactly as imagined from cavitation phenomena. Without cavitation the pressure drops as far as orifice 2, then the pressure rises.

The zero pressure lines are dashes, with the p/q values plotted upward. The location of the zero lines was so chosen that they are lower by p_a/q than a fixed ordinate point.

Visualizing the cavitation as nonexistent, the pressure curve in this representation would then remain the same at constant q , regardless of the value of p_a - that is, the depth of the zero line. Then at a reduction of pressure p_a the zero line shifts upward and ultimately meets this fixed pressure curve. This representation shows that up to the line of intersection of the zero line with the original pressure curve there exists a stage with constant low pressure, and that from there on the pressure rises. This affords empirical reference points for the expected shock positions at given velocity and given outside pressure. Accordingly, there remains in first approximation (at constant pressure) the pressure curve without cavitation, and at incipient cavitation the piece below the particular zero line is simply cut off.

On the whole, it results in a very intimate relation between the processes in wind tunnels and on airfoils, the judicious application of which may prove quite advantageous for further experimental studies.

It might be added that the start of cavitation is accompanied by a rattling, detonating noise which, at high velocities and angles of attack, changed to a very loud noise even in this small setup. The propeller noise of ship screws operating with cavitation is well known, so also the apprehensive roar of turbines operating with excessively high suction gradient.

4. Sphere Tests

These experiments and observations were made on a 20-millimeter sphere mounted in the center of the square test channel. A pressure orifice permitted the measurement along a whole circle, the sphere being rotatable from the outside about the spindle axis; but, since the spindle had to be fairly thick (4.5 mm) for reasons of strength, the symmetry of flow was nevertheless perceptibly affected. (See fig. 31.)

The observations disclosed the following: when the pressure drops at constant speed, bubbles begin to form behind the body in the vortex cores, rather than on the surface as on the airfoil; at still further reduction of pressure the bubbles begin to form on the body itself, and ultimately become quite pronounced, as seen from the short-time photograph. (See fig. 32.)

Separation starts directly behind the equator. At a distance of about one sphere diameter the shock is again visible, followed by a gleam caused by small bubbles. Under still further pressure reduction complete separation takes place, appearing as a perfectly transparent tube filled with water vapor trailing aft of the body. (See fig. 33.)

The pressure measurements (fig. 34) yield the following: the forward stagnation point corresponds to the angle $\varphi = 0$, the rear one to $\varphi = 180^\circ$; $\frac{p - p_a}{q}$ is plotted as ordinate.

Curve a refers to the noncavitational stage, b for the stage corresponding to figure 32, and c for the stage of figure 33. The asymmetry caused by the spindle is probably the reason of the maximum depression exceeding the theoretical minimum (-1.25), as, in fact, subsequent checks confirmed. The effect of the adjacent walls is a slight increase of velocity estimated at about 5 percent at the sphere equator.

The drag coefficients, defined by

$$W = c_w \frac{\pi}{4} D^2 \frac{\rho}{2} w_\infty^2 \quad (12)$$

are obtained by graphical integration over the sphere surface; no allowance being made for the asymmetry nor for the effect of tangential friction.

Stage a gives $c_w = 0.48$

Stage b gives $c_w = 0.57$

Stage c gives $c_w = 0.49$

If, with a given outside pressure, say, atmospheric pressure, for instance, the velocity is continuously increased, the curves b, c would gradually change into one similar to d, because the atmospheric pressure is very low compared to the then very high dynamic pressure. The lowest negative value of p/q then signifies cavitation so that practically only the positive part of the pressure curve remains significant.

Here a comparison with Bauer's experiments are of interest. (See reference 12.) He shot steel balls of about 11 millimeters in diameter at rates of between 150 and 650 meters per second through water and measured the resistance electrically by determining the deceleration.* The dynamic pressure rises to around 2200 atmospheres at 650 meters per second; equally great tensile stresses would have to be expected if the pressure curve were of type a. Actually, however, cavitation sets in; the ball shoots a hole in the water. This drag coefficient is 0.30 (according to the present definition). Curve d also would give 0.30 and may therefore represent in some degree the pressure distribution in Bauer's experiments. Naturally, it is not permissible to compare these c_w values with those obtained in the wind tunnel at the same Reynolds number; the cavitation is not adaptable to Reynolds' law of analogy.

*His calculation of the resistance from deceleration records in water is afflicted with an error, insofar as he ignored the inertia of water which causes an apparent sphere mass enlargement. In potential flow the apparent mass enlargement of a sphere amounts to half the displaced water mass; but here it becomes certainly less, so that the actual error might amount to several percent in the sense of higher resistance.

III. THEORETICAL CONSIDERATIONS

1. Preliminary Remarks

Mere observation of the cavitation processes shows very plainly their turbulent character, and with that the rather unlikely promise of making more progress with theoretical considerations than afforded from actual experiments. In what follows it is attempted to find a somewhat rational explanation for the facts observed in part II. The most elementary means are employed. As long as the present empirical knowledge is not greater, it would not serve much useful purpose to make the calculations more rigorous.

Thus it appears possible to explain the process, called compression shock, mechanically. (See sec. 4.) Furthermore, if the shock layer is assumed to be thicker, sensible values result.

The travel of the position of the shock is readily established; the theoretically deduced pressure distribution in the closed channel is largely in agreement with the observed.

Lastly, it is found that, on passage of the bubbles through the shock area, an almost instantaneous pressure change actually takes place, which the theories of mechanical corrosion had heretofore assumed without sufficient mechanical basis. The estimation of the maximum pressures in the subsequent compression of the bubbles (sec. 4) affords values according to which the extremely severe corrosion, which often occurs, can be traced back to mechanical effects. The considerations of section 6 regarding experiments elsewhere indicate that the calculated pressures might be high enough for it. Here the present empirical knowledge is particularly incomplete. Hence any speculations which could be easily made would be premature.

2. Compression Shock in the Bubble Mixture

The most important result of the experiments described in part II appears to be the identification of the shock processes. In the earlier so-called compression shock the pressure jumps by considerable amounts, whereby bubbles disappear almost entirely,

It suggests itself to place this compression process on a parallel with the uniform Riemann gas compression shock, which occurs when gas with supersonic velocity strikes an obstacle. Admittedly, the mixture of water and vapor bubbles manifests a relatively coarse structure; hence the ensuing considerations refer to statistical average values.

It is admissible to speak of sonic velocity even in connection with such mixtures, provided the propagation of audible signals, which obviously would be very complicated, is discounted.

Visualize a 1-cubic-centimeter mixture containing x -parts by volume of air or vapor and $(1 - x)$ parts of water. The density of the mixture is accurately enough expressed with $\rho_0 (1 - x)$, where ρ_0 equals the density of pure water, or in other words, the gas mass is disregarded as being vanishing. On the other hand, it is obviously permissible to visualize the elasticity of the mixture as being solely caused by the enclosed gases - that is, to exclude the small elasticity of the water.

The velocity of sound a , the rate of propagation of small disturbances, is, generally,

$$a = \sqrt{\frac{dp}{d\rho}} \quad (13)$$

It can be expressed numerically, if $p = f(\rho)$ is known - that is, make a statement regarding the physical changes accompanying the passage of the small disturbance.

Assuming, to begin with, a polytrope, namely:

$$p x^m = \text{constant}$$

then

$$x = 1 - \frac{\rho}{\rho_0}$$

leads to

$$\frac{dp}{d\rho} = a^2 = \frac{m p}{\rho_0 x}$$

or

$$a = \sqrt{\frac{m p}{\rho_0 x}} \quad (14)$$

If, for instance, $p = 2 \times 10^4$ dynes per square centimeter (≈ 0.02 atmosphere); $\rho_0 = 1$ gram per cubic centimeter; $x = 0.05$ and $m = 1.20$, then $a = 692$ centimeters per second. This is a readily obtainable velocity; hence the appearance of compression shocks seems perfectly feasible.

3. The Straight Compression Shock

The premises are: a system of coordinates solidly connected with the plane of the shock, a rigorously uniform shock; ρ_1 equals density, u_1 velocity, p_1 pressure, and x_1 vapor content before the shock, and ρ_2 , u_2 , p_2 , and x_2 the corresponding values after the shock. The gas mass is always disregarded relative to the water mass.

Then the equation of continuity gives

$$\rho_1 u_1 = \rho_2 u_2 \quad (15)$$

the momentum equation:

$$\rho_1 u_1 (u_1 - u_2) = p_2 - p_1 \quad (16)$$

The energy equation should be added as the third; it would state essentially that compression heat is released during the shock. But this heat is transferred through the pipe on to the water, which becomes heated to a usually negligible degree. Then, if the control area for equations (15) and (16) is kept far enough away from the place of the shock, isothermal processes must be assumed and

$$\frac{x_1}{x_2} = \frac{p_2}{p_1} \quad (17)$$

substitutes for the energy formula.

From equations (15) and (16) there follows:

$$\rho_1 u_1^2 \left(1 - \frac{p_1}{p_2}\right) = p_2 - p_1$$

Then the introduction of $\frac{p_2}{p_1} = s$, gives $\frac{x_1}{x_2} = s$, and with it:

$$\left. \begin{aligned} \frac{\rho_1 u_1^2 x_1}{p_1} \left(\frac{1 - 1/s}{1 - x_1/s} \right) &= s - 1 \\ \text{and} \\ s &= x_1 \left(1 + \frac{\rho_1 u_1^2}{p_1} \right) = x_1 \left(1 + \frac{\rho_0 (1 - x_1) u_1^2}{p_1} \right) \end{aligned} \right\} \quad (18)$$

To illustrate: for

$$\rho_1 = \rho_0 (1 - x_1) = 0.95 \text{ gram per cubic centimeter}$$

$$u_1 = 4000 \text{ centimeters per second} = 40 \text{ meters per second}$$

$$p_1 = 2 \times 10^4 \text{ dyn per square centimeter}$$

$$s = 38$$

A very considerable compression has taken place.

Given u_1 and p_1 , s becomes maximum for

$$x'_1 = \frac{1}{2} \left(1 + \frac{p_1}{\rho_0 u_1^2} \right) \quad (19)$$

Since the second summand in parenthesis is always small, $x'_1 \approx \frac{1}{2}$. If the bubbles are visualized as spheres

$$x_1 = \frac{\pi \sqrt{2}}{6} = 0.74 \text{ is obtained for the densest packing;}$$

hence the previously calculated value of x'_1 is possible. Now it seems that x_1 assumes lower values.

The highest water velocities employed in engineering probably range around 150 meters per second. For $x_1 = 0.5$ and $p = 1 \times 10^4$ dyn per square centimeter, the highest feasible pressure ratio is $s = 5625$; and hence $p_2 \approx 56$ atmospheres.

It is not very likely that such pressures would produce mechanical corrosion directly. Hence the theories

assuming mechanical corrosion must provide further a mechanism that raises these pressures to an entirely different order of magnitude. (See sec. 4.) Equation (18) is hardly suitable for water vapor since condensation occurs. But, at the same time, it is readily apparent that the pressure rise, even by complete condensation, varies but very little from that established with equation (18); which results in:

$$s = 1 + \frac{\rho_0 u_1^2 (1 - x_1) x_1}{p_1} \quad (20)$$

4. Structure of Plane Compression Shock

The calculation so far afforded a summary prediction of the processes accompanying the shock. The final stage after the shock was obtained from the stage before the shock. Now an attempt is made to explore the intermediate values and, in particular, to compute the thickness of the shock area.

Visualize moving along with a bubble. The shock is accompanied by the approach of a pressure rise wherein the shock actually occurs not mathematically nonuniform but rather over a relatively great distance. The bubble thus becomes a little smaller, the pressure in it increases as a result of the compression of vapor. It is essential that the outside pressure is not, in general, completely in accord with that on the inside and for the following reason:

Continuity demands

$$\rho u = \text{constant}$$

The momentum theory gives for the outside pressure p_a

$$\rho_1 u_1 (u_1 - u) = p_a - p_1$$

or, when introducing x :

$$\rho_0 (1 - x_1) u_1^2 \frac{x_1 - x}{1 - x} = p_a - p_1 \quad (21)$$

Now there exists between x and p_i the pressure within the bubble, a relation which is given through heat conduction, evaporation, and so forth. If p_i were identical to p_a , this relation would have to have precisely the form of equation (21), which naturally in no way can occur. Rather, the process is such that at first the interval pressure lags behind the outside pressure and later overhauls it. The pressure difference acts to accelerate or decelerate the collapsing motion of the bubble.*

Now it would be extremely difficult to solve the simultaneous system of equations, which, on one hand, defines the inside pressure, and on the other, contains equation (21), because the time factor becomes an essential element in the equation for the inside pressure (heat conduction).

The problem can be materially simplified by specifying the relation between p_i and x , perhaps in polytropic form with, for the present, arbitrary exponent m . In that case, p_i is known for each x , and, according to the momentum theory, or equation (21), respectively, the outside pressure p_a as well. The pressure difference $p_a - p_i$ compresses the bubble. The exponent of the polytropes must be determined from a special consideration. The bubble is to remain spherical during the contraction, which is possible only when the shock area is great compared to the radius of the bubble.

Let r equal the radius of a round bubble at a certain time interval. The radial motion of the surrounding water during the contraction is given by

$$v_r = \frac{dr}{dt} \left(\frac{r}{s} \right)^2 \quad (22)$$

*The conditions are similar to those in Riemann's gas shock; if assumed uniform. There, the pressure calculated from the equation of continuity and momentum theory does not, at first, agree with the pressure obtained from the gas equation, when the temperature is defined according to the energy formula. The explanation in this case is found in the friction stresses which cannot be neglected relative to the gas pressure.

where r is the radius of the spherical bubble at a certain time interval and s is the distance of a point from the center. The kinetic energy of the total water mass is

$$E = \frac{\rho_0}{2} \int_{s=r}^{s=\infty} 4\pi s^2 \frac{r^4}{s^4} \left(\frac{dr}{dt}\right)^2 ds = \frac{\rho_0}{2} \left(\frac{dr}{dt}\right)^2 4\pi r^3 \quad (23)$$

which, with the new variable $\xi = \frac{r}{r_1}$, (r_1 equals initial radius), and $v_1 = \frac{4}{3} \pi r_1^3$, gives:

$$E = \frac{\rho_0}{2} 3v_1 r_1^2 \xi^3 \left(\frac{d\xi}{dt}\right)^2 \quad (24)$$

Then the work performed by the pressures is computed.

a. Outside pressure p_a . - According to equation (21):

$$p_a = p_i + \rho_0 u_1^2 (1 - x_1) \frac{(x_1 - x)}{(1 - x)}$$

In general, x and x_1 are small with respect to unity; hence it is permissible in the prediction of the period of collapse to put $\frac{1 - x_1}{1 - x}$ approximately equal to unity.

Then

$$p_a = p_i + \rho_0 u_1^2 (x_1 - x) \quad (25)$$

For a cubic centimeter containing n bubbles, each of volume v_1

$$nv = x$$

that is

$$nv_1 = x_1$$

and

$$p_a = p_i + \rho_0 u_1^2 nv_1 \left(1 - \frac{v}{v_1}\right)$$

or

$$p_a = p_i + \rho_0 u_1^2 x_1 (1 - \xi^3) \quad (26)$$

The variation of p_a is indicated by the curve ACB in figure 35.

b. Interval pressure p_1 .— The interval pressure follows the law of polytropic change

$$p_1 v_1^m = p_1 v^m \quad (27)$$

or

$$\frac{p_1}{p_1} = \left(\frac{v}{v_1}\right)^{3m} \quad (27a)$$

with m as the polytropic exponent. The curve ACD of figure 35 was obtained.

As the bubble becomes smaller the pressures perform work, the difference of which is utilized to raise or lower the kinetic energy E of the water around the bubble. From

$$E = - \int_{v_1}^v (p_a - p_1) dv = - \int_{\xi=1}^{\xi} (p_a - p_1) v_1 3 \xi^2 d\xi$$

there follows, after insertion of p_a from equation (26) and of p_1 from equation (27a):

$$E = p_1 v_1 (\alpha + \beta \xi^3 + \gamma \xi^6 + \delta \xi^{-3m+3}) \quad (28)$$

whereby

$$\left. \begin{aligned} \alpha &= 1 + \frac{1}{m-1} + \frac{\rho_0 u_1^2 x_1}{2p_1} \\ \beta &= - \left(1 + \frac{\rho_0 u_1^2 x_1}{p_1} \right) \\ \gamma &= \frac{\rho_0 u_1^2 x_1}{2p_1} \\ \delta &= - \frac{1}{m-1} \end{aligned} \right\} \quad (29)$$

By equating E according to equations (24) and (28) there is obtained after elementary transformations:

$$\frac{d\xi}{dt} = \frac{\sqrt{\alpha\xi + \beta\xi^4 + \gamma\xi^7 + \delta\xi^{-3m+4}}}{r_1\xi^2 \sqrt{\frac{3p_0}{2p_1}}} \quad (30)$$

and

$$t = \sqrt{\frac{3p_0}{2p_1}} r_1 \int_{\xi}^{\xi=1} \frac{\xi^2 d\xi}{\sqrt{\alpha\xi + \beta\xi^4 + \gamma\xi^7 + \delta\xi^{-3m+4}}} \quad (31)$$

Accordingly, if u_1 , x_1 , p_1 , and m are given, the time interval for the collapse of the bubble to a certain fraction ξ of its original radius increases in proportion to the radius itself.

Since m can assume any value between 1 and 1.4 in diatomic gases, a closed integration is impossible, but the graphical method is available. In any case the integrand near the zero places can be developed and approximate expressions established.

The pertinent zero places are:

1. $\xi_1 = 1$, the starting point
2. $\xi_2 = \xi < 1$, the stage of maximum compression of the bubble that is of interest from the point of view of pressure and temperature. In point of fact, there the linear contraction velocity disappears

$$r_1 \frac{d\xi}{dt} = \sqrt{\frac{2p_1}{3p_0}} \frac{\sqrt{\alpha\xi + \beta\xi^4 + \gamma\xi^7 + \delta\xi^{-3m+4}}}{\xi^2} \quad (32)$$

The solution $\xi_1 = 1$ can be directly verified; ξ_2 is, as will be shown later, so small in all practical cases, that ξ^4 and ξ^7 can be neglected.

But then

$$\alpha\xi_2 = -\delta\xi_2^{-3m+4} \quad (33)$$

or, with equation (29):

$$\xi_2 = \left(\frac{1}{m + (m-1) \frac{\rho_0 u_1^2 x_1}{2p_1}} \right)^{\frac{1}{3(m-1)}} \quad (33a)$$

At ξ_1 and ξ_2 the graphical integration fails, because the integrand becomes infinite, and approximate terms must be developed.

Putting $\xi = 1 - \sigma$ in proximity of the starting point, where σ is to be very small compared to unity, the integrand of equation (31) is

$$\frac{(1 - \sigma)^2}{\sqrt{\alpha(1 - \sigma) + \beta(1 - \sigma)^4 + \gamma(1 - \sigma)^7 + \delta(1 - \sigma)^{-3m+4}}}$$

It is readily seen that in the development of $(1 - \sigma)^n$ according to powers of σ , quadratic terms must be included. For, in first approximation, the root assumes the value zero.

In second approximation

$$dt = \sqrt{\frac{3\rho_0}{2p_1}} r_1 \frac{(1 - 2\sigma + \sigma^2) d\sigma}{\sqrt{\frac{9}{2} \left(\frac{\rho_0 u_1^2 x_1}{p_1} - m \right) \sigma^2}}$$

and, accurately enough, for the direct proximity of ξ_1 :

$$t_{1,2} = \sqrt{\frac{\rho_0}{3p_1}} r_1 \frac{1}{\sqrt{\frac{\rho_0 u_1^2 x_1}{p_1} - m}} \lg \frac{\sigma_2}{\sigma_1} \quad (34)$$

If $\xi = 1$ and $\sigma_1 = 0$, $t_{1,2}$ becomes logarithmically

infinite, which physically means that without impulse by a suitable disturbance the shock is not started. But, if a slight compression $\sigma > 0$ already exists, the bubble collapses very quickly.

In the vicinity of ξ_2 the root again becomes very small. The integrand is approximately

$$\frac{\xi^2}{\sqrt{\alpha\xi + \delta\xi^{-3m+4}}}$$

With $\xi = \xi_2(1 + \sigma)$ the integrand becomes

$$\frac{\xi_2^2(1 + \sigma)^2}{\sqrt{\alpha\xi_2(1 + \sigma) + \delta\xi_2^{-3m+4}(1 + \sigma)^{-3m+4}}}$$

and, according to equation (33), with allowance only of the first power of σ :

$$\frac{\xi_2^2(1 + 2\sigma)}{\sqrt{3\alpha\xi_2(m-1)\sigma}}$$

The integration with this integrand gives

$$t_{3,4} = \sqrt{\frac{2\rho_0}{p_1}} r_1 \frac{\xi_2^3}{\sqrt{\alpha\xi_2(m-1)}} \sigma^{1/2} \left(1 + \frac{2}{3}\sigma\right)^{3/2} \quad (35)$$

Then, if the transitional zone is graphically integrated, the collapse can be traced in respect to time.

For instance, with

$$u = 4000 \text{ centimeters per second; } m = 4/3$$

$$p_1 = 2 \times 10^4 \text{ dyn. per square centimeter; } x_1 = 0.05,$$

values which are feasible in practice, and where the exponent $4/3$ for water vapor would almost give adiabatic compressions; thus by equation (29)

$$\alpha = 24; \quad \beta = -41; \quad \gamma = 20; \quad \delta = -3$$

and, by equation (31):

$$t = \sqrt{\frac{3p_0}{2p_1}} r_1 \int_{\xi_2}^1 \frac{\xi^2 d\xi}{\sqrt{24\xi - 41\xi^4 + 20\xi^7 - 3}}$$

By equation (33), $\xi_2 = \frac{1}{8}$. With consideration to the logarithmic character of equation (34), $\xi = 0.99$ is chosen as the starting point and the interval time $t_{1,2}$ computed according to equation (34) with $\xi = 0.90$ as the second limit.

In proximity of ξ_2 the integrand has the form

$$\frac{\xi^2}{\sqrt{24\xi - 3}}$$

with a minimum at $\xi = \frac{1}{6}$. This is the location of the highest linear compression velocity

$$r_1 \frac{d\xi}{dt} = \sqrt{\frac{p_1}{p_0}} 29.4$$

The time interval from $\xi = \frac{1}{6}$ to state of rest $\xi_2 = \frac{1}{8}$ is calculated graphically according to equation (35), between $\xi = \frac{1}{6}$ and $\xi = 0.90$.

By knowing the time interval for each x and ξ , the local variation of the compression is readily ascertained. In the time interval dt the bubble travels the distance $dl = u dt$ or, in bubble radii,

$$\frac{dl}{r_1} = \frac{u dt}{r_1} = \frac{u_1(1-x_1)}{(1-x)} \frac{dt}{r_1} = \frac{u_1(1-x_1)}{(1-x_1\xi^3)} \frac{dt}{r_1}$$

which, with equation (31), gives:

$$\frac{dl}{r_1} = u_1 \frac{1 - x_1}{1 - x_1 \xi^3} \sqrt{\frac{3\rho_0}{2p_1}} \frac{\xi^2 d\xi}{\sqrt{\alpha\xi + \beta\xi^4 + \gamma\xi^7 + \delta\xi^{-3m+4}}} \quad (36)$$

Since $r = r_1 \xi$, the compression can be completely indicated (fig. 36); it essentially takes place over a very short distance; the pressure jumps over a distance of $4.2r_1$ to about 2700 fold. The bubble diameters are also shown in figure 36. The temperature rises considerably; with a maximum of 2300° absolute the heat conduction must obviously play an important part and the exponent m must certainly be quite remote from the adiabatic. For the point at issue the correct choice of m is not important. The compression very likely is not purely polytropic. The present lack of knowledge of the heat condition of bubbles likewise precludes any exact prediction as to what occurs when the stage of maximum compression is exceeded. The cooling naturally is very pronounced; the simultaneously resultant condensation of the hot vapor depends upon the heat transferred to the water.

Besides, neither the presence of other bubbles nor the fact that the bubbles do not have to collapse concentrically is considered; they possibly could be stretched and torn by the locally widely varying pressures. All these problems need to be followed up in much more exact experimental studies of the individual processes. Hence the decision to omit the results of a fairly comprehensive analysis concerning the approximate solution of the heat conduction problem at this time, except for a tabulation of the maximum pressure and temperatures at different u_1 , x_1 , and m , which are of interest with regard to the corrosion theories.

The equation

$$\xi_2 = \frac{r_2}{r_1} = \left(\frac{1}{m + (m-1) \frac{\rho_0 u_1^2 x_1}{2p_1}} \right)^{\frac{1}{3(m-1)}}$$

was found valid for small values of x . From comparison with the polytropic formula

$$\frac{v_2}{v_1} = \left(\frac{T_1}{T_2} \right)^{\frac{1}{m-1}}$$

follows

$$\frac{T_2}{T_1} = m + (m - 1) \frac{\rho_0 u_1^2 x_1}{2p_1}$$

Carrying the approximation further

$$\frac{T_2}{T_1} = m + (m - 1) \frac{\rho_0 u_1^2 x_1 (1 - x_1)}{2p_1} \quad (37)$$

hence, in known manner:

$$\frac{p_2}{p_1} = \left(\frac{T_2}{T_1} \right)^{\frac{m}{m-1}}$$

Tables 14 and 15 show very plainly that powerful pressures and temperatures are to be expected at the shock areas, even if the numerical values are recognized only in order of magnitude.

Calculations of the pressures accompanying the collapse of bubbles from the point of view of cavitation phenomena have been made repeatedly (reference 13; also reports by H. Föttinger and D. Thoma of reference 1), but always on the more or less vague assumption that the pressure outside the bubble was somehow greater than on the inside, and so caused a collapse. It always involved either completely empty bubbles - that is, a vacuum (Parsons and Cook, also Rayleigh) or else isothermal changes (Rayleigh, Föttinger). However, it may be stated, on the basis of the present investigation, that the prerequisite for the collapse (namely, the very rapid variation of the outside pressure) has now been established. And one of the first problems now consists in ascertaining whether the corrosion actually occurs, as it seems, at the place of the collapse. Nearly all the available experiments, although very numerous, are obtained in practical operation, where the conditions for a clearly defined shock position probably never are exactly complied

with. At any rate, it is very well known in practice that the corrosion occurs behind the spot at which cavitation begins.

5. Compression Shocks in Channels

The processes in divergent channels described in the preceding chapters can, to some extent, be treated mathematically; in particular, it is possible to grasp the shifting of the shock areas in flow direction under decreasing back pressure.

The actual process is visualized somewhat schematized. The separation is to start in the narrowest section E-E (fig. 37) and abate completely at the shock area S-S; the pressure rise is to occur in a relatively small area from A-A to B-B, where F is the cross-sectional area at B-B and w is the average velocity. The friction is disregarded.

Since the pressure from E-E to A-A is very approximately equal to zero, the assumption that B-B lies very close to A-A, gives, with the momentum formula,

$$\rho_0 w_0^2 F_0 = \rho_0 w^2 F + \Delta p_1 F$$

For simplicity it is assumed that the space filled by bubbles contains very little water.

$$\text{Since } F_0 w_0 = F w,$$

$$\Delta p_1 = \rho_0 w_0^2 \left(\frac{F_0}{F} - \left(\frac{F_0}{F} \right)^2 \right) \quad (38)$$

The relative pressure jump $\frac{\Delta p_1}{\frac{1}{2} \rho_0 w_0^2}$ computed for the small test nozzle in figure 38 according to equation (38) is indicated by dashes. This discontinuous pressure rise has a maximum $\Delta p_1 = \frac{1}{2} \frac{\rho_0}{2} w_0^2$ at $\frac{F_0}{F} = \frac{1}{2}$. As the cross section after the shock continues to expand, a

second gradual pressure rise occurs, which is calculated according to Bernoulli

$$\Delta p_2 = \frac{\rho_0}{2} (w^2 - w_2^2) = \frac{\rho_0}{2} w^2 \left\{ 1 - \left(\frac{F}{F_2} \right)^2 \right\} \quad (39)$$

The plotting of this pressure rise then gives a picture which qualitatively corresponds to the test data in figures 9 and 10, except for the smoothed transitions. The pressure jump deduced from the pressure measurements

in figure 15 equals $0.33 \frac{\rho_0 w_0^2}{2}$, while at the point where the pressure was measured, it should, at the most,

amount to about $0.45 \frac{\rho_0 w_0^2}{2}$. Even the variation of the

pressure curves after shock is closely reproduced in figure 38.

The place of the shock on the suction side of an airfoil travels, in principle, the same way; save that a summary treatment, as in the closed channel, is not possible.

6. Appendix

The Destructive Effect of Short-Period Shock Stresses

In connection with the previously cited mechanical corrosion theories, the experiments by E. Honegger (reference 14) are of interest.

He studied the strength of various structural materials against corrosion under violently impinging water droplets. His method consisted in moving test bars mounted on a fast rotating disk at high speed against one or more jets of water. He found that the weight loss due to corrosion is no longer perceptible at relative speeds of $v < 125$ meters per second, and at speeds of $v > 125$ meters per second can be represented approximately by $a(v - 125)^2$, where a is constant.

When a flat surface strikes a cylindrical jet of water running parallel to it, only the particles directly adjacent to the point of impact are accelerated at the

moment of impact; those farther away do not feel the motion change. The conditions are exactly as in the pressure line of a water-power plant when the discharge opening is suddenly closed. Alliévi's theory (reference 15) may be applied. But it is necessary, if more than the first approximation is to be made, to consider the rate of propagation of the pressure as being dependent on the order of magnitude of the pressure jump rather than constant.

A system of coordinates is used in which the shock wave rests. For reasons of simplicity it is further assumed that the process is linear - that is, such as occurs in a pressure resistant pipe, for instance. This is permissible, since only the maximum pressure value is considered.

"If the water, viewed absolute, is at rest, while the wall moves with velocity v , then, if u is the rate of propagation of the shock, the relative velocities are

$$w_1 = u \quad \text{and} \quad w_2 = u - v$$

The equation of continuity gives

$$\rho_1 w_1 = \rho_2 w_2$$

the momentum equation:

$$\rho_1 w_1 (w_1 - w_2) = p_2 - p_1 = \Delta p = \rho_1 u v$$

The elimination of v leaves

$$u = \sqrt{\frac{\rho_2}{\rho_1} \frac{\Delta p}{\Delta \rho}} \quad (40)$$

if $\Delta p = p_2 - p_1$ and

$$u - v = \sqrt{\frac{\rho_1}{\rho_2} \frac{\Delta p}{\Delta \rho}} \quad (41)$$

For small pressure jumps, the expressions in equations (40) and (41) change to sonic velocity $a = \sqrt{\frac{dp}{d\rho}}$, because

$\rho_2 \approx \rho_1$ and the quotients of the differences must be replaced by differential quotients.

But an attempt at an actual prediction of u is predicated on the knowledge of the physical changes accompanying the shock. Strictly speaking, the energy equation is sufficient, but the lack of knowledge of the specific heat of the coefficients of expansion, and so forth, at the ensuing high pressures call for a simplification which is permissible provided the pressures are not excessive ($p < 10,000$ atmospheres). It readily can be proved that the heating of the fluid on impact is not so great that the isothermic pressure-volume curve obtained by Bridgman (reference 16) up to very great pressures (fig. 39) could no longer be properly used. Next calculate u and $u-v$ for any one point of the curve according to equations (40) and (41) or, conversely, begin with the velocity v and obtain the pressure jumps Δp . (See fig. 40.) The pressures are comparatively small. It is surprising, nevertheless, that such a hard and tough metal as chromium-nickel steel is so severely attacked, especially when considering that the true pressures in the test could scarcely have been higher than those in figure 40, since the pressure waves are reflected with the inverse sign from the free surface of the water jet and tend to reduce.

The results are equally applicable to the subject of the present investigation to the extent that a very similar type of stress is involved at the severe, rapidly changing cavitation shocks. The maximum pressure at $v = 125$ meters per second is around 2100 kilograms per square centimeter, and is reached according to table 15, at 40 meters per second water speed; $m = 1.2$; $x_1 = 0.06$. The behavior of ordinary grey pig iron is worthy of note. Its low resistance under practical cavitation stresses, as in Honegger's experiments, is surprising. Honegger ascertained a marked dependence on the jet thickness and, specifically, that thinner jets were less effective. Perhaps the air entrained by the rotating disk sets the thin jets into motion even before the shock and that the relative velocity is reduced; however, a more detailed discussion of this problem is without the scope of the present report.

After completion of this article, Muëller (reference 17) published some experiments which may be considered as a continuation of those described here. Its outstanding feature is the collection of clear photographs of the bubbles and the compression shock obtained with a Thun slow-motion picture camera.

Translation by J. Vanier,
National Advisory Committee
for Aeronautics.

REFERENCES

1. Hydraulische Probleme, Vorträge auf der Hydraulik-Tagung in Göttingen, 1925. VDI-Verlag (Berlin), 1926, p. 101. Also contains reports on Cavitation by H. Föttinger, D. Thoma, W. Wagenbach, M. Schilhansl, and J. Ackeret.
2. Lamb, Horace: Hydrodynamics. The Univ. Press, Cambridge, (Eng.), 6th ed., 1932.
3. Flamm, O.: Die Schiffsschraube und ihre Wirkung auf das Wasser (München und Berlin), 1909.
4. Prandtl, L.: Göttinger Nachr. Math.-phys. Klasse, 1918, p. 107.
5. Ergebnisse der aerodynamischen Versuchsanstalt zu Göttingen. Lfg. 1 (München und Berlin), 1921.
6. Kirchhoff, G.: Vorlesungen über Mechanik 1876, p. 186.
7. Meyer, J.: Abhandlungen d. deutsch. Bunsen-Ges., Halle, No. 6, 1911.
8. Camerer: Vorlesungen über Wasserkraftmasch. (Leipzig und Berlin), 2d ed., 1924, p. 51.
9. Stodola, A.: Die Dampfturbinen. 4th ed. (Berlin), 1910, p. 70.

10. Dubs, R.: Wasserkraft-Jahrbuch. München, 1924, p. 440.
Andres, K.: Forschungsarbeiten auf dem Gebiete des
Ingenieurwes., no. 76, 1909.
11. Von Helmholtz, H.: Monatsberichte d. Akad. D. Wiss.
(Berlin), 1868, p. 125.
12. Bauer, W.: Ann. d. Phys., (4) vol. 80, 1926, p. 232;
vol. 82, 1927, p. 1014.
13. Parsons, C. A., and Cook.: Engineering, 1919, p. 515.
Rayleigh: Scientific Papers, vol. 6, p. 504.
14. Honegger, E.: BBC-Mitteilungen, April 1927, p. 95.
15. Alliévi-Dubs: Veränderliche Bewegung des Wassers in
Leitungen. Berlin, 1909.
16. Landolt-Börnstein: Physikalisch-Chemische Tabellen,
5th ed., vol. 1, 1923, p. 77 ff.
17. Mueller, H.: Naturwissenschaften, 1928, p. 423.

Table I. Pressure distribution on the back wall of the nozzle.
(Pressure in mm of water.)

p_0	p_a	q	p_1	p_2	p_3	p_4	p_5	p_6	p_7	p_8	p_9	p_{10}
23.68	0.55	22.65	0.38	0.09	0.34	0.48	0.82	1.24	2.00	4.30	5.97	6.91
28.53	5.39	22.67	6.82	11.05	14.89	16.24	17.22	18.07	18.74	19.67	20.31	20.87
23.8	0.53	22.80	0.38	0.18	2.77	6.00	8.35	9.85	10.81	12.27	13.20	13.88
19.11	0.49	18.21	0.27	0.08	0.51	0.95	1.85	3.01	4.07	6.03	6.95	7.71
19.11	0.45	18.25	0.27	0.07	0.30	1.21	2.39	3.62	4.81	6.76	7.81	8.49
19.11	0.46	18.24	0.27	0.08	0.65	1.48	2.74	4.21	5.40	7.18	8.27	8.93
19.11	0.46	18.24	0.27	0.07	1.07	2.37	4.11	5.66	6.70	8.27	9.22	9.85
19.11	0.46	18.24	0.20	0.08	2.22	4.48	6.40	7.61	8.36	9.54	10.48	11.07
19.11	0.46	18.24	0.16	1.55	7.17	8.49	9.51	10.26	10.77	11.78	12.39	13.12
22.38	3.42	18.57	4.68	8.11	11.20	12.24	13.10	13.78	14.35	15.18	15.77	16.24

Table II. Pressure distribution in shock. (Pressure in m of water column)

p_0	p_a	q	p_{11}	p_{12}	p_{13}	p_{14}	p_{15}
18.60	1.50	16.75	9.85	10.38	10.78	11.16	11.47
18.22	0.81	17.05	8.05	8.69	9.28	9.62	10.09
18.22	0.83	17.01	6.52	7.48	8.12	8.65	9.12
18.22	0.91	16.92	3.42	4.91	6.41	7.23	7.86
18.22	0.92	16.91	1.62	2.96	4.33	5.74	6.82
18.22	0.92	16.91	0.92	2.22	3.23	4.70	5.89
18.33	0.80	17.15	0.44	0.72	1.60	2.51	4.15
18.30	0.80	17.12	0.45	0.62	1.01	1.58	2.80
18.22	0.96	16.90	0.37	0.50	0.64	0.75	0.96

Table III. Distribution of pressure rise in shock.

Shock reaches to points	$\frac{p_{12}-p_{11}}{q}$	$\frac{p_{13}-p_{11}}{q}$	$\frac{p_{14}-p_{11}}{q}$	$\frac{p_{15}-p_{11}}{q}$
11	0.038	0.069	0.092	0.120
12	0.056	0.092	0.123	0.150
13	0.088	0.175	0.224	0.261
14	0.079	0.160	0.243	0.306
15	0.077	0.136	0.223	0.293
16	0.017	0.067	0.121	0.216
17	0.010	0.033	0.066	0.137
18	0.008	0.016	0.022	0.035

Table IV. Coefficients for airfoil A.

α_∞	C_a	C_D	$\epsilon = \frac{C_D}{C_a}$	C_m
-8.9°	-0.026	0.018	-0.67	0.11
-6.7	0.17	0.015	0.085	0.15
-5.6	0.28	0.014	0.049	0.18
-4.5	0.38	0.014	0.037	0.20
-3.5	0.49	0.013	0.026	0.22
-2.3	0.57	0.012	0.022	0.25
-1.1	0.67	0.011	0.017	0.27
-0.1	0.77	0.011	0.014	0.29
+1.0	0.88	0.013	0.015	0.32
2.1	0.96	0.017	0.017	0.34
4.5	1.13	0.025	0.022	0.38
6.9	1.27	0.034	0.027	0.43
9.7	1.32	0.071	0.054	0.47

Table V. Coefficients for airfoil B.

α_∞	C_a	C_D	$\epsilon = \frac{C_D}{C_a}$	C_m
-10.8°	-0.30	0.095	-0.32	-0.031
-8.3	-0.16	0.019	-0.12	-0.054
-6.1	0.037	0.015	0.41	0.10
-5.1	0.14	0.014	0.10	0.12
-4.0	0.23	0.0136	0.059	0.14
-2.8	0.34	0.013	0.039	0.17
-1.8	0.44	0.013	0.030	0.19
+0.5	0.64	0.0125	0.020	0.25
2.6	0.84	0.015	0.018	0.30
4.9	1.02	0.019	0.019	0.34
7.3	1.17	0.028	0.024	0.37
9.0	1.26	0.055	0.044	0.40

Table VI. Coefficients for airfoil C.

α_∞	C_a	C_D	$\epsilon = \frac{C_D}{C_a}$	C_m
-7.7°	-0.32	0.082	-0.26	-0.052
-5.6	-0.12	0.043	-0.36	-0.062
-3.3	0.093	0.02	0.21	0.14
-2.2	0.19	0.014	0.078	0.15
-1.1	0.28	0.011	0.038	0.17
0	0.38	0.007	0.02	0.20
1.1	0.47	0.008	0.017	0.22
3.3	0.62	0.016	0.026	0.23
5.8	0.81	0.03	0.037	0.27
8.3	0.94	0.066	0.070	0.30
9.3	0.95	0.091	0.097	0.32
11.4	0.90	0.15	0.17	0.35

Table VII. Coefficients for airfoil D.

α_∞	C_a	C_D	$\epsilon = \frac{C_D}{C_a}$	C_m
-7.3°	-0.43	0.083	-0.19	-0.11
-5.1	-0.21	0.045	-0.22	-0.01
-3.1	0.019	0.019	1.01	0.088
-2.0	0.12	0.013	0.10	0.11
-0.9	0.23	0.009	0.04	0.14
+0.2	0.33	0.007	0.022	0.16
1.5	0.40	0.010	0.025	0.17
3.7	0.59	0.018	0.031	0.21
5.9	0.77	0.037	0.048	0.24
7.5	0.88	0.070	0.081	0.29
8.5	0.88	0.093	0.106	0.31
11.7	0.83	0.16	0.19	0.33

Table IX. $p_{a,q}$ values for different stages of cavitation on airfoils, A and B. (A_2 indicates airfoil A, α , 20° ; the other designations are accordingly.)

		Start		edge		Separation	
		q	p_a	q	p_a	q	p_a
$A_2 \dots$	{	1,64	3,00	1,48	2,02	1,40	1,18
		2,48	4,50	2,46	3,40	2,38	1,56
		4,06	6,64	4,08	5,51	3,91	2,40
		7,07	11,48	6,90	9,10	6,77	3,50
		10,10	15,40	10,00	13,01	9,49	4,75
$A_5 \dots$	{	1,21	2,68	1,26	2,04	0,97	0,88
		1,98	4,21	1,99	3,25	1,88	1,37
		3,81	7,40	3,60	5,41	3,67	2,42
		6,09	12,12	5,74	7,94	6,81	4,31
		8,01	15,34	7,61	12,80	9,78	5,92
		10,18	19,81	9,60	14,21	—	—
$B_2 \dots$	{	2,42	3,43	2,38	2,33	2,85	1,39
		2,46	3,58	2,43	2,19	3,33	1,68
		4,41	6,50	5,39	5,56	3,37	1,68
		8,07	11,85	7,76	6,45	3,56	1,77
		9,00	13,09	8,65	7,18	5,04	2,55
		10,61	14,69	10,10	9,21	6,65	3,53
		10,72	15,93	11,62	9,752	8,72	4,08
		12,38	17,97	13,80	11,34	9,66	4,56
		14,37	19,83	—	—	11,28	5,22
		14,52	21,70	—	—	13,60	6,44
$B_5 \dots$	{	1,07	2,29	0,83	0,90	0,71	0,65
		2,14	4,60	2,02	2,05	—	—
		2,94	4,72	2,28	2,49	2,19	1,38
		3,69	7,12	3,82	5,05	3,91	2,39
		3,81	7,00	4,51	6,80	6,75	4,11
		8,47	14,84	8,20	11,31	8,65	5,23
		10,78	20,14	10,70	15,01	11,00	6,52
		14,55	26,50	13,00	17,18	12,85	7,72

	$x =$	0,02	0,05	0,10	0,20
$m = 1,1$	$u = 20 \text{ m/s}$	1,3	1,6	2,0	2,7
	40	1,9	3,1	4,7	7,5
	80	4,3	9,1	15,5	—
$m = 1,2$	$u = 20$	1,6	2,2	3,0	4,4
	40	2,8	5,2	8,4	14,0
	80	7,6	17,2	—	—
$m = 1,3$	$u = 20$	1,9	2,8	4,0	6,1
	40	3,7	7,3	12,1	—
	80	10,9	—	—	—
$m = 1,4$	$u = 20$	2,2	3,4	5,0	7,8
	40	4,6	9,4	—	—
	80	14,2	—	—	—

	Start Trailing edge					Start Trailing edge					Start Trailing edge			
	<i>q</i>	<i>p_a</i>	<i>q</i>	<i>p_a</i>		<i>q</i>	<i>p_a</i>	<i>q</i>	<i>p_a</i>		<i>q</i>	<i>p_a</i>	<i>q</i>	<i>p_a</i>
<i>C</i> ₂ ..	2.51	1.77	2.47	1.42	<i>D</i> ₂ ..	3.21	2.42	3.16	2.02	<i>E</i> ₂ ..	1.70	0.78	1.54	0.50
	3.76	2.67	3.88	1.87		5.56	3.92	5.85	3.08		1.75	0.96	3.44	1.78
	5.57	4.14	5.77	2.92		6.25	4.88	6.46	3.46		3.84	2.88	4.88	2.89
	8.60	6.84	8.85	4.22		8.58	6.00	8.80	4.28		4.75	3.86	7.18	3.28
	9.89	6.68	9.75	4.89		10.80	7.70	10.48	5.04		7.78	5.55	8.75	4.67
	18.22	9.29	14.10	6.84		15.40	10.32	12.13	6.38		8.56	6.09	9.75	4.60
<i>C</i> ₅ ..	1.61	2.48	1.54	1.46	<i>D</i> ₅ ..	1.68	2.71	1.58	1.62	<i>E</i> ₅ ..	12.57	9.42	—	—
	2.18	3.29	2.16	2.09		3.42	5.50	3.38	3.85		1.15	2.08	1.16	1.01
	2.96	4.29	2.88	3.03		3.49	5.76	3.40	3.68		2.86	4.79	2.87	2.55
	3.85	4.77	4.47	4.19		6.25	10.32	4.86	4.72		4.95	7.88	4.78	4.70
	5.19	7.79	6.94	7.31		8.84	13.89	4.91	5.82		8.21	13.92	8.14	6.97
	6.97	10.44	8.25	8.34		10.18	16.62	8.88	7.59		8.50	15.67	8.44	7.66
<i>C</i> ₇ ..	7.46	10.745	13.80	14.01	<i>D</i> ₇ ..	—	—	9.60	9.40	<i>E</i> ₇ ..	8.68	15.84	9.74	8.22
	8.40	12.26	—	—		1.08	2.46	0.98	1.17		10.04	17.80	12.24	10.08
	10.45	15.27	—	—		2.68	5.89	2.61	3.39		12.52	21.29	—	—
	12.90	20.44	—	—		4.21	9.34	5.77	7.13		0.505	1.23	1.865	2.33
	—	—	—	—		6.20	13.96	5.88	8.25		1.94	4.31	2.87	3.32
	—	—	—	—		7.96	18.35	7.58	10.07		2.94	6.93	4.47	4.89
<i>C</i> ₂ ..	0.68	1.46	1.185	1.61	<i>D</i> ₂ ..	8.80	19.48	8.60	11.71	<i>E</i> ₂ ..	8.09	19.38	7.94	9.12
	1.32	3.16	2.56	3.16		10.70	24.03	10.48	14.28		9.90	22.86	8.59	9.62
	2.62	5.78	3.415	4.31		—	—	—	—		—	—	9.51	11.29
	3.59	7.38	3.58	5.265		—	—	—	—		—	—	—	—
	6.25	13.18	4.80	6.15		—	—	—	—		—	—	—	—
	7.22	15.68	6.99	8.14		—	—	—	—		—	—	—	—
<i>C</i> ₅ ..	8.77	18.50	8.44	10.87	<i>D</i> ₅ ..	—	—	—	—	<i>E</i> ₅ ..	—	—	—	—
	10.82	22.45	10.25	12.935		—	—	—	—		—	—	—	—

Table XI. Values $\lambda = p_a - p_d / q$ for different stages of cavitation and different airfoils.

Airfoil	A_2	A_5	B_2	B_5	C_2	C_5	C_7	D_2	D_5	D_7	E_2	E_5	E_7
Start	1.62	1.90	1.48	1.79	0.69	1.44	2.09	0.71	1.61	2.20	0.75	1.69	2.80
Trailing edge	1.29	1.45	0.85	1.87	0.46	1.05	1.25	0.47	0.90	1.86	0.50	0.84	1.18
Separation	0.46	0.58	0.46	0.58	—	—	—	—	—	—	—	—	—

Table XII. Pressure measurements on airfoils A and B.

	$p_o - p_a$	p_a	p_1	p_2	p_3	p_4	p_5	p_a	p_1	p_2	p_3	p_4	p_5
								$p_o - p_a$	$p_o - p_a$	$p_o - p_a$	$p_o - p_a$	$p_o - p_a$	$p_o - p_a$
A_2 $t_w = 16.5^\circ \text{C}$	8.39	4.16	0.30	0.31	0.31	0.31	0.21	0.496	0.086	0.037	0.037	0.037	0.025
	8.45	9.165	0.31	0.28	0.32	1.07	2.66	1.085	0.037	0.033	0.038	0.127	0.315
	8.725	13.75	0.29	0.31	0.35	5.75	9.92	1.576	0.033	0.036	0.04	0.66	1.137
						7.58						0.87	
A_5 $t_w = 16.5^\circ \text{C}$	8.00	14.88	1.48	0.915	4.08	7.04	10.95	1.86	0.185	0.114	0.511	0.88	1.37
							10.76						1.344
	7.74	4.91	0.26	0.30	0.31	0.28	0.32	0.635	0.034	0.039	0.04	0.036	0.041
	7.79	9.45	0.25	0.28	0.57	1.44	2.20	1.214	0.032	0.036	0.511	0.185	0.283
B_2 $t_w = 16^\circ \text{C}$							2.05						0.264
	8.19	16.335	0.24	0.30	0.53	8.08	12.62	2.00	0.029	0.037	0.065	0.99	1.54
						10.16						1.24	
	8.14	23.32	2.13	4.71	11.42	16.30	20.78	2.87	0.261	0.579	1.38	2.00	2.55
B_5 $t_w = 16^\circ \text{C}$							20.02						2.46
	7.54	16.10	4.30	5.18	8.21	10.13	13.03	2.14	0.57	0.687	1.09	1.344	1.73
						10.25						1.36	
	7.59	10.505	0.22	0.20	0.69	6.66	7.71	13.85	0.029	0.026	0.091	0.878	1.015
C_2 $t_w = 16^\circ \text{C}$						6.41						0.845	
	7.36	7.255	0.19	0.21	0.46	0.56	2.13	0.985	0.026	0.029	0.063	0.076	0.289
	7.59	3.11	0.71	0.21	0.26	0.28	0.29	0.41	0.094	0.028	0.034	0.037	0.038
C_5 $t_w = 16^\circ \text{C}$	7.41	19.62	0.84	5.48	9.94	13.275	16.93	2.65	0.113	0.74	1.34	1.79	2.286
				5.23	10.44					0.705	1.41		
	7.59	16.78	0.24	0.35	8.80	10.38	13.845	2.21	0.032	0.046	1.16	1.368	1.826
				8.17							1.076		
C_7 $t_w = 16^\circ \text{C}$	7.25	11.235	0.33	0.33	1.05	2.20	4.96	1.54	0.046	0.046	0.145	0.304	0.685
	6.95	4.26	0.24	0.26	0.36	0.26	0.24	0.614	0.035	0.037	0.052	0.037	0.035

Table XIII. Pressure measurements on airfoils C, D, and E.

	$p_o - p_a$	p_a	p_1	p_2	p_3	p_a	p_1	p_2	p_3
						$p_o - p_a$	$p_o - p_a$	$p_o - p_a$	$p_o - p_a$
C_2 $t_w = 16^\circ \text{C}$	8.06	21.37	9.18	9.36	10.25				1.27
					10.13	2.65	1.138	1.16	1.256
	8.01	15.38	1.34	2.53	2.36	1.92	0.167	0.316	0.295
C_5 $t_w = 16^\circ \text{C}$	7.95	13.175	0.295	0.30	0.30	1.66	0.037	0.038	0.038
	8.03	21.54	16.33	16.37	18.13	2.68	2.017	2.1	2.26
	8.075	20.44	6.03	5.98	7.00	2.54	0.748	0.741	0.868
C_7 $t_w = 16^\circ \text{C}$	7.89	16.72	0.55	0.84	1.86	2.12	0.07	0.107	0.236
	7.29	16.39	11.51	11.70	12.84	2.25	1.58	1.61	1.764
	7.54	15.40	10.38	10.65	11.89	2.04	1.377	1.413	1.578
D_2 $t_w = 13.2^\circ \text{C}$	7.31	8.075	0.58	1.19	2.38	1.105	0.079	0.163	0.326
	6.88	11.78	8.88	8.83	9.01	1.71	1.29	1.283	1.31
	6.68	4.31	1.51	1.32	1.70	0.645	0.226	0.198	0.255
E_2 $t_w = 13.2^\circ \text{C}$	6.78	0.30	0.265	0.275	0.28	0.045	0.039	0.041	0.042
	6.68	3.61	0.18	0.26	0.26	0.54	0.027	0.039	0.039
	7.21	5.505	2.78	2.86	3.17	0.763	0.379	0.397	0.44
E_5 $t_w = 13.2^\circ \text{C}$	7.31	19.71	17.12	17.15	17.44	2.7	2.34	2.35	2.39
	6.68	3.77	0.22	0.24	0.285	0.565	0.033	0.036	0.043
	6.96	11.68	8.32	8.33	8.985	1.678	1.195	1.197	1.29
	7.1	20.37	16.95	17.12	17.67	2.87	2.39	2.414	2.49

Table XV. p_2/p_1 against T_2/T_1 and m

	$T_2/T_1 = 2$	4	6	8	10
$m = 1.1$	2070	4.27×10^6	3.63×10^6	3.75×10^9	10^{11}
1.2	64.0	4096	4.65×10^4	2.62×10^5	10^6
1.3	20.2	408	2350	8130	2.14×10^4
1.4	11.5	127	524	1440	3170

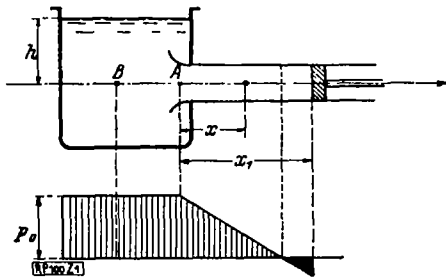


Figure 1.- Negative pressures produced by acceleration.

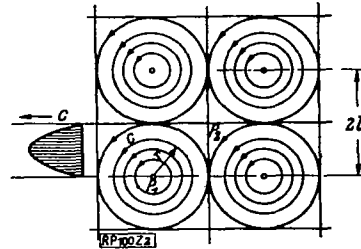


Figure 2.- Vortex curves in turbulent motion.

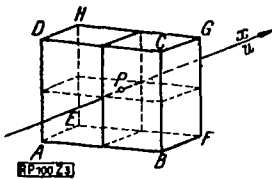


Figure 3.- Parallelepiped flat in stream direction.

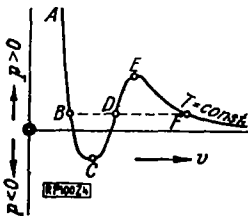


Figure 4.- Van der Waals isotherm.

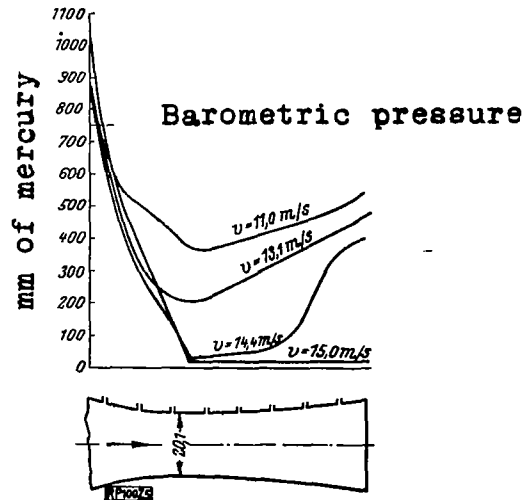


Figure 5.- Preliminary nozzle tests.

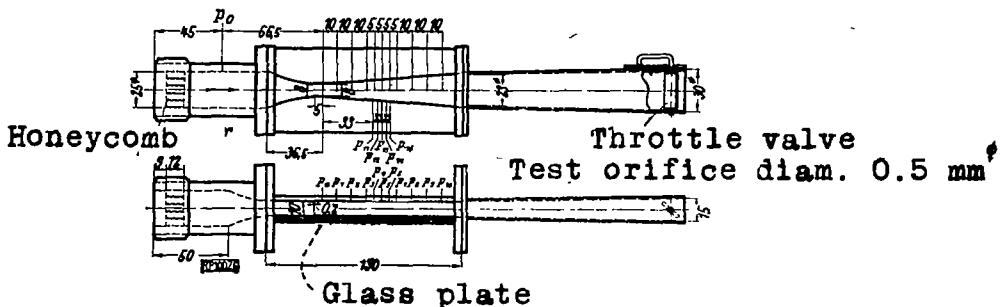


Figure 6.- Test nozzle with pressure taps.

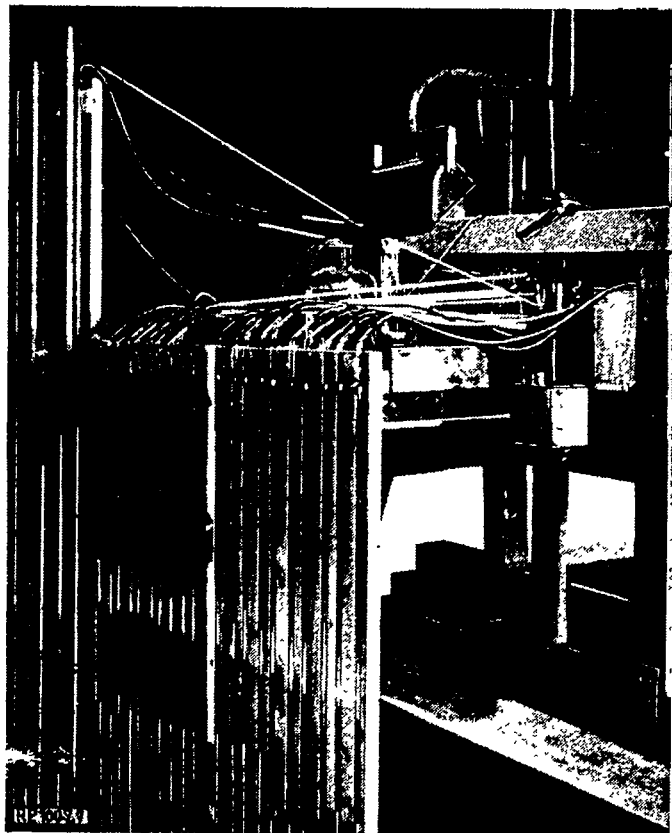


Figure 7.-
Set-up
of test
nozzle
and
manometer.

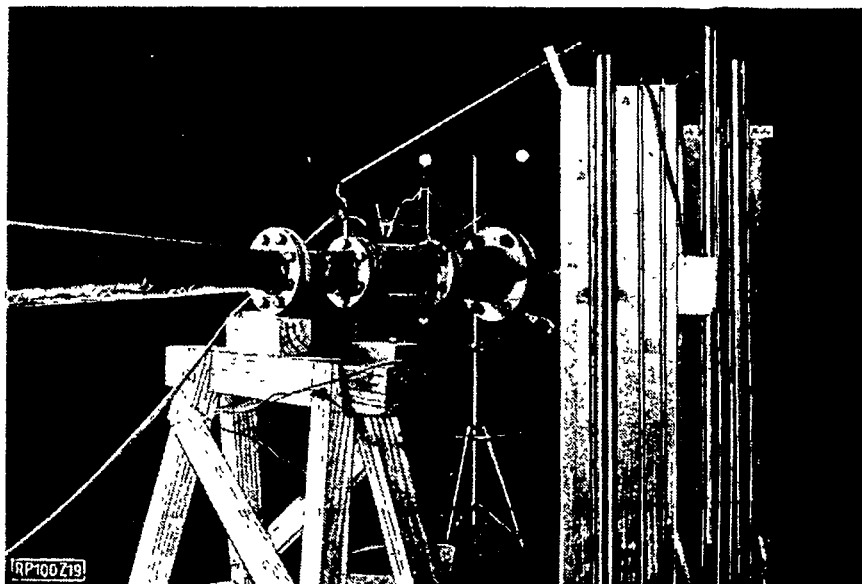


Figure 19.- Experimental arrangement.

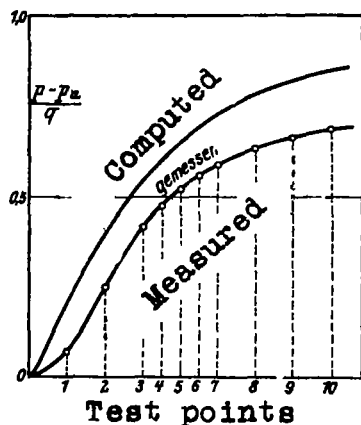


Figure 8.- Pressure rise in flow without cavitation.

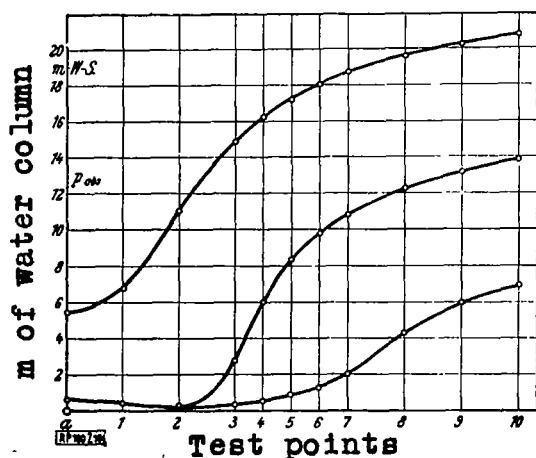
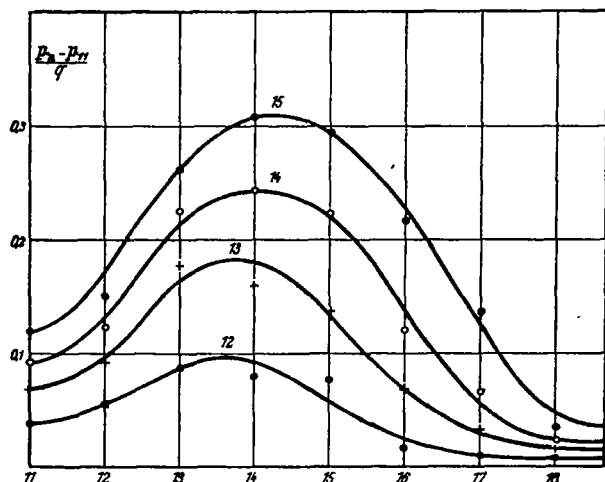


Figure 10.- Pressure at through flow of 1.69 l/s with different throttling.



Mean range of shock, test points

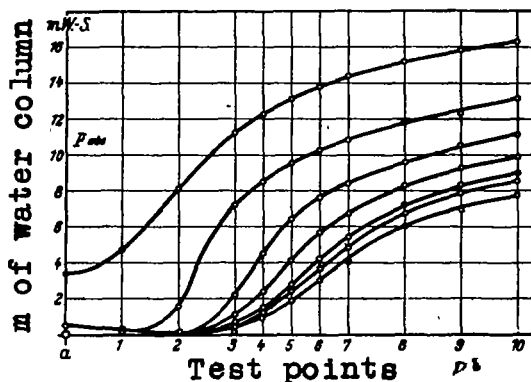


Figure 9.- Pressure at through flow of 1.47 l/s with different throttling.

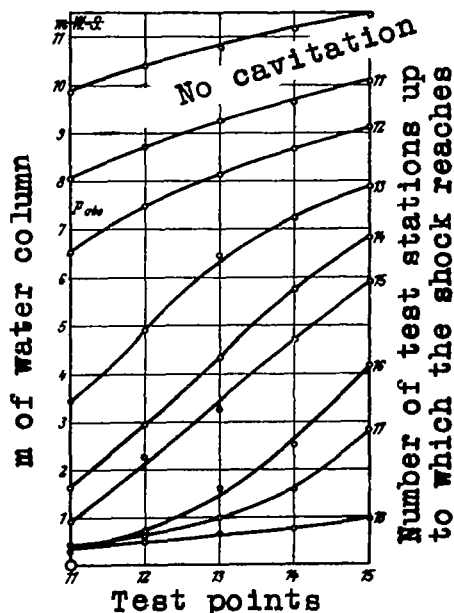


Figure 13.- Pressures at different positions of pressure pumps.

Figure 14.- Relative pressure rise (direct measurement).



Figure 11.- Film records of bubble formation in divergent channel, severe throttling.



Figure 12.- Film records of bubble formation in divergent channel, slight throttling.

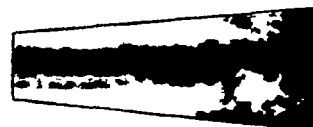
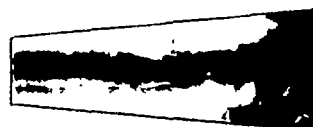


Figure 32.- Bubble formation behind sphere.

Figure 33.- Cavitation behind sphere.

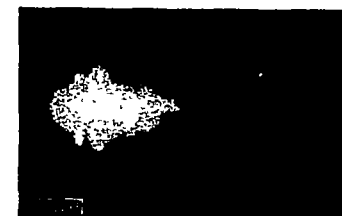


Figure 22.-Airfoil A. Start of separation.



Figure 23.-Airfoil A. Separation extends beyond trailing edge.



Figure 24.-Airfoil A. Complete separation.

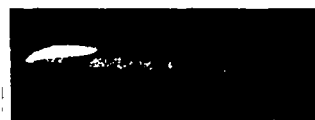
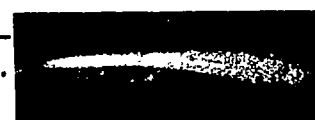


Figure 25.- Airfoil C. Separation to 1/4 chord.

Figure 26.- Airfoil C. Separation beyond trailing edge.



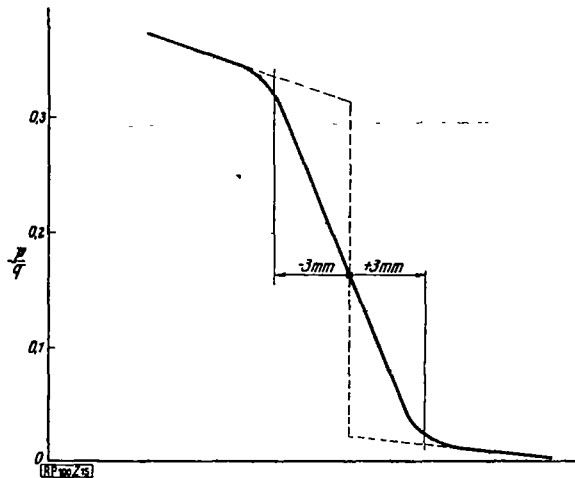
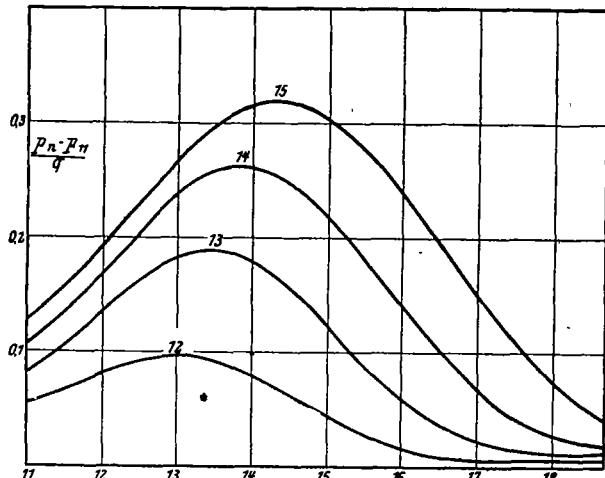


Figure 15.- Hypothetical form of pressure pump.



Mean range of shock, test points

Figure 16.- Relative pressure rise (by assumed form of pressure pump of fig.15).

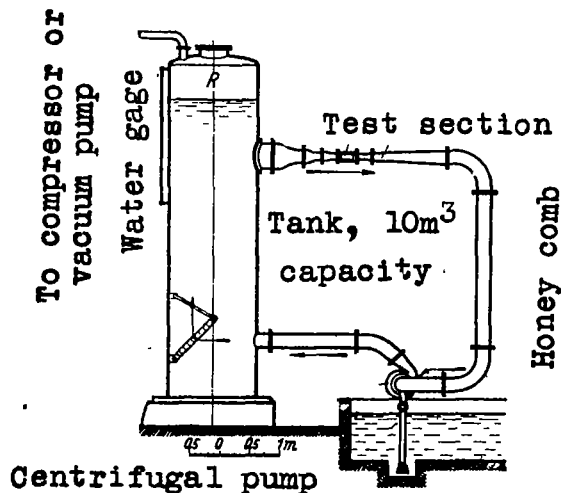


Figure 17.- General arrangement of the large cavitation-test plant.

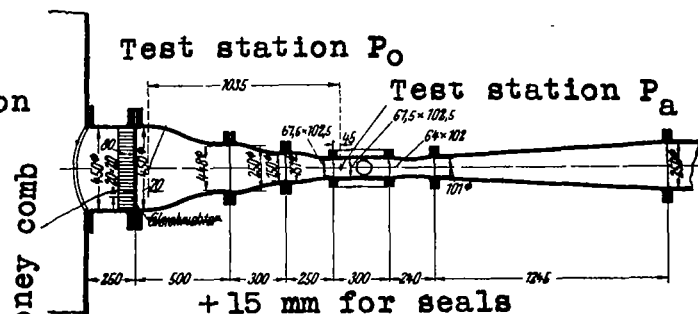


Figure 18.- Test section for cavitation.

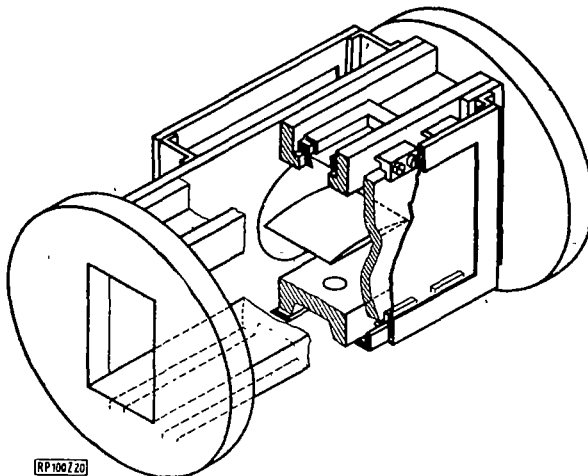
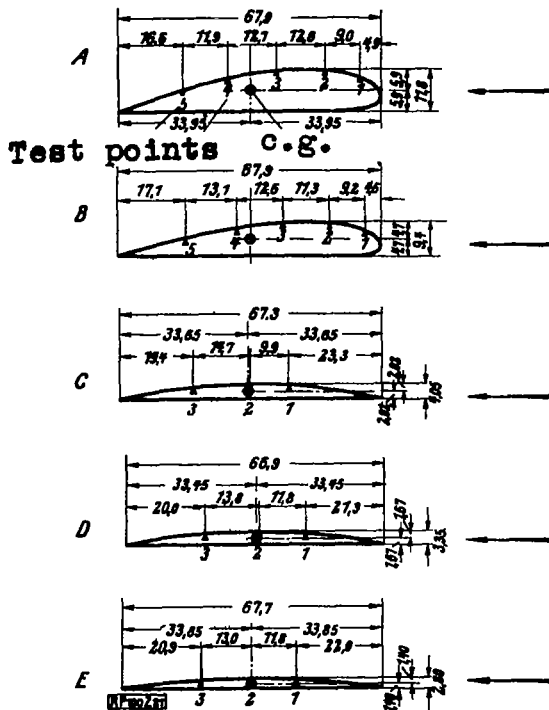


Figure 20.- Frame for attaching airfoils.



- No cavitation
- + Shock at 1/3t chord
- Shock at chord t
- Separation

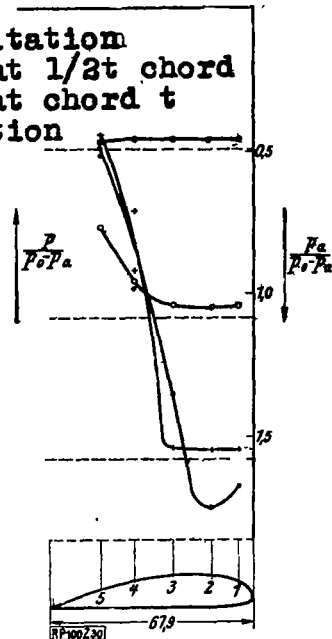


Figure 30.- Pressure distribution on suction side of airfoil A at 2° angle of attack (A_2).

Figure 21.- Airfoil sections.

- Start
- + Trailing edge
- Separation

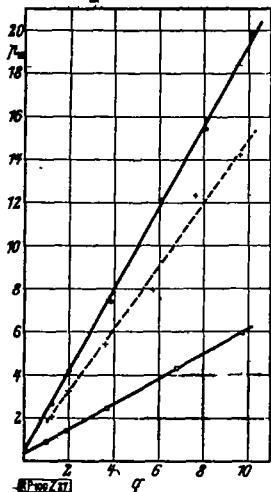


Figure 27.- p-q plot for airfoil A at $\alpha = 5^\circ$.

- Start
- + Trailing edge
- Separation

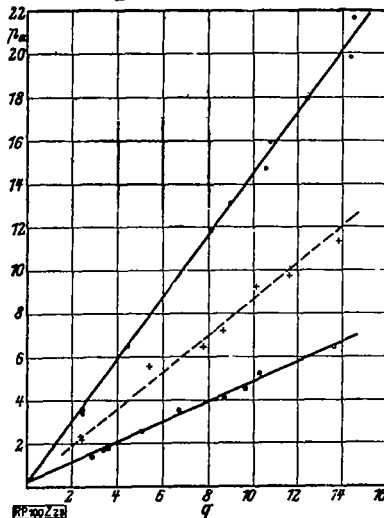


Figure 28.- p-q plot for airfoil B at $\alpha = 2^\circ$.

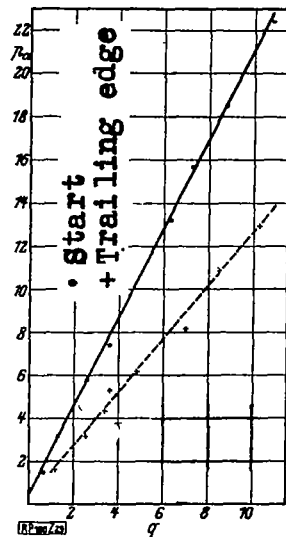


Figure 29.- p-q plot for airfoil C at $\alpha = 7^\circ$.

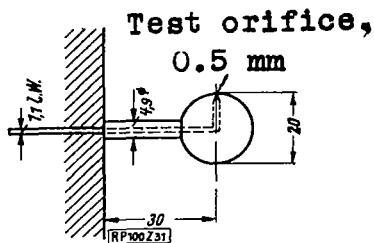
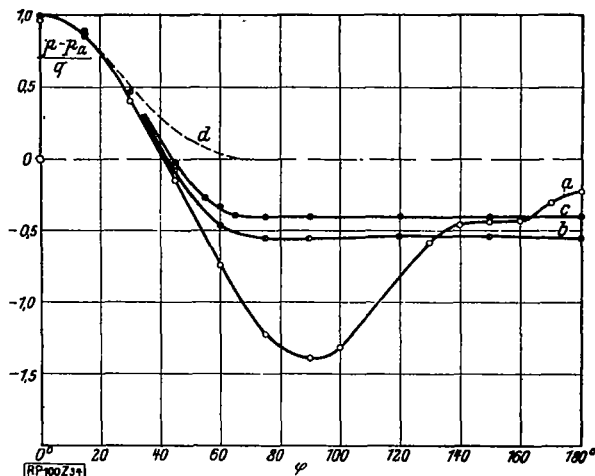


Figure 31.-
Arrangement
of experimental
sphere.



- (a) Without cavitation.
- (b) Cavitation as in fig. 32.
- (c) Cavitation as in fig. 33.

Figure 34.- Pressure measure-
ments on sphere.

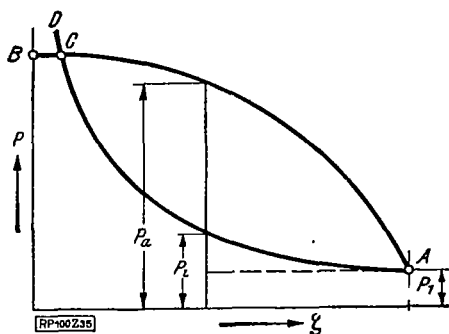


Figure 35.- Variation
of inside
and outside pressure.

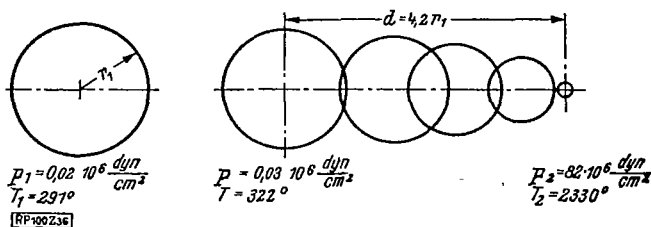


Figure 36.- Size of bubbles
during shock.

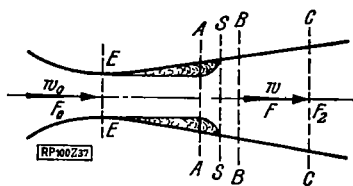


Figure 37.- Shock process in a channel.

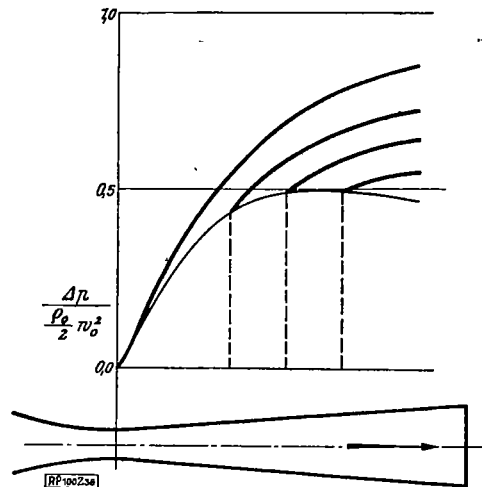


Figure 38.- Pressure distribution in a channel computed for different back pressures.

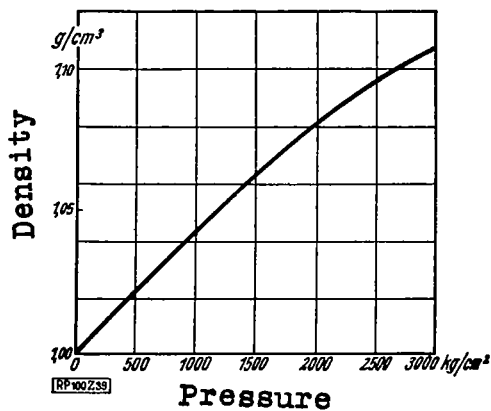


Figure 39.- Density of water plotted against pressure (Bridgman).

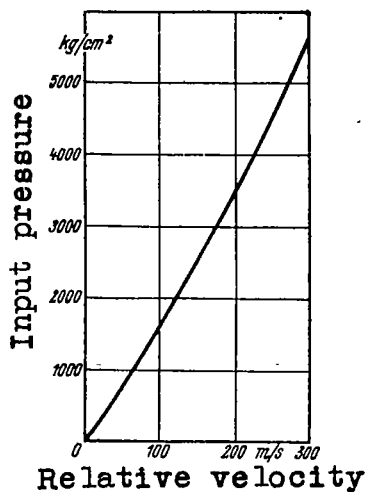


Figure 40.- Shock pressure plotted against relative velocity.



3 1176 01440 7846

7

Source of NASA

T M 1078

Candace

Candace - 1000

Candace - 1000

Candace - 1000

Candace

Candace - 1000

Candace - 1000

Candace - 1000

Candace - 1000